

This work was written as part of one of the author's official duties as an Employee of the United States Government and is therefore a work of the United States Government. In accordance with 17 U.S.C. 105, no copyright protection is available for such works under U.S. Law.

Public Domain Mark 1.0











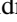





<https://creativecommons.org/publicdomain/mark/1.0/>

Access to this work was provided by the University of Maryland, Baltimore County (UMBC) ScholarWorks@UMBC digital repository on the Maryland Shared Open Access (MD-SOAR) platform.

**Please provide feedback**

Please support the ScholarWorks@UMBC repository by emailing [scholarworks-group@umbc.edu](mailto:scholarworks-group@umbc.edu) and telling us what having access to this work means to you and why it's important to you. Thank you.

# Ninety-seven Eclipsing Quadruple Star Candidates Discovered in TESS Full-frame Images

Veselin B. Kostov<sup>1,2,3</sup> , Brian P. Powell<sup>1</sup> , Saul A. Rappaport<sup>4</sup> , Tamás Borkovits<sup>5,6,7</sup> , Robert Gagliano<sup>8</sup> , Thomas L. Jacobs<sup>9</sup> , Martti H. Kristiansen<sup>10</sup> , Daryll M. LaCourse<sup>11</sup> , Mark Omohundro<sup>12</sup>, Jerome Orosz<sup>13</sup> , Allan R. Schmitt<sup>14</sup> , Hans M. Schwengeler<sup>15</sup>, Ivan A. Terentev<sup>16</sup>, Guillermo Torres<sup>17</sup> , Thomas Barclay<sup>1,18</sup> , Adam H. Friedman<sup>1,19</sup>, Ethan Kruse<sup>1</sup> , Greg Olmschenk<sup>1,20</sup> , Andrew Vanderburg<sup>21</sup> , and William Welsh<sup>13</sup> 

<sup>1</sup> NASA Goddard Space Flight Center, 8800 Greenbelt Road, Greenbelt, MD 20771, USA; [veselin.b.kostov@nasa.gov](mailto:veselin.b.kostov@nasa.gov)

<sup>2</sup> SETI Institute, 189 Bernardo Ave, Suite 200, Mountain View, CA 94043, USA

<sup>3</sup> NASA Goddard Space Flight Center Sellers Exoplanet Environments Collaboration, USA

<sup>4</sup> Department of Physics, Kavli Institute for Astrophysics and Space Research, Massachusetts Institute of Technology, Cambridge, MA 02139, USA

<sup>5</sup> Baja Astronomical Observatory of University of Szeged, H-6500 Baja, Szegedi út, Kt. 766, Hungary

<sup>6</sup> Konkoly Observatory, Research Centre for Astronomy and Earth Sciences, H-1121 Budapest, Konkoly Thege Miklós út 15-17, Hungary

<sup>7</sup> ELTE Gothard Astrophysical Observatory, H-9700 Szombathely, Szent Imre h. u. 112, Hungary

<sup>8</sup> Amateur Astronomer, Glendale, AZ 85308, USA

<sup>9</sup> Amateur Astronomer, 12812 SE 69th Place, Bellevue, WA 98006, USA

<sup>10</sup> Brorfelde Observatory Observator, Gyldenkeres Vej 7, DK-4340 Tølløse, Denmark

<sup>11</sup> Amateur Astronomer, 7507 52nd Place NE, Marysville, WA 98270, USA

<sup>12</sup> Citizen Scientist, c/o Zooniverse, Department of Physics, University of Oxford, Denys Wilkinson Building, Keble Road, Oxford, OX1 3RH, UK

<sup>13</sup> Department of Astronomy, San Diego State University, 5500 Campanile Drive, San Diego, CA 92182, USA

<sup>14</sup> Citizen Scientist, 616 W 53rd Street, Apt. 101, Minneapolis, MN 55419, USA

<sup>15</sup> Citizen Scientist, Planet Hunter, Bottmingen, Switzerland

<sup>16</sup> Citizen Scientist, Planet Hunter, Petrozavodsk, Russia

<sup>17</sup> Center for Astrophysics | Harvard & Smithsonian, 60 Garden Street, Cambridge, MA, 02138, USA

<sup>18</sup> University of Maryland, Baltimore County, 1000 Hilltop Circle, Baltimore, MD 21250, USA

<sup>19</sup> University of Michigan, 500 S State Street, Ann Arbor, MI 48109, USA

<sup>20</sup> Universities Space Research Association, 7178 Columbia Gateway Drive, Columbia, MD 21046, USA

<sup>21</sup> Department of Astronomy, University of Wisconsin–Madison, Madison, WI 53706, USA

Received 2022 January 5; revised 2022 February 4; accepted 2022 February 9; published 2022 April 13

## Abstract

We present a catalog of 97 uniformly vetted candidates for quadruple star systems. The candidates were identified in TESS full-frame image data from sectors 1–42 through a combination of machine-learning techniques and visual examination, with major contributions from a dedicated group of citizen scientists. All targets exhibit two sets of eclipses with two different periods, both of which pass photocenter tests confirming that the eclipses are on target. This catalog outlines the statistical properties of the sample, nearly doubles the number of known multiply eclipsing quadruple systems, and provides the basis for detailed future studies of individual systems. Several important discoveries have already resulted from this effort, including the first sextuply eclipsing sextuple stellar system and the first transiting circumbinary planet detected from one sector of TESS data.

*Unified Astronomy Thesaurus concepts:* Multiple stars (1081); Eclipsing binary stars (444)

*Supporting material:* machine-readable table

## 1. Introduction

Half of Sunlike stars are members of binary systems (Raghavan et al. 2010), and about one in 10 of these are triples and quadruples (Tokovinin 2018). The higher-order multiplicity fraction increases with stellar mass, to the point where massive single stars are an exception rather than the norm (e.g., Moe & Di Stefano 2017). Multiple stellar systems are important tracers of stellar formation, can experience rich interactions such as Lidov-Kozai oscillations (Lidov 1962; Kozai 1962) or dynamical instability, and provide pathways for important stages of stellar evolution such as short-period binaries, common-envelope events, Type Ia Supernovae, and black hole mergers (e.g., Pejcha et al. 2013; Fang et al. 2018; Fragione & Kocsis 2019; Liu & Lai 2019; Hamers et al. 2021).

For example, the mass ratios between the individual components of a quadruple system, the period ratios between the constituent binary systems, and the mutual inclination provide important insight into whether the system formed through a “top-down” scenario via core or disk fragmentation or “bottom-up” aggregation via gravitational capture (e.g., Mathieu 1994; Whitworth 2001; Pineda et al. 2015; Tobin et al. 2016; Tokovinin 2021). In addition, the evolution of a compact quadruple stellar system can include a combination of single-star evolution and interactions between the two stars in the constituent binary systems, as well as dynamical interactions between the two binary systems. Detection and characterization of eclipsing binary stars (EBs) in quadruple stellar systems provide an excellent opportunity to explore these processes (e.g., Borkovits et al. 2016; Rappaport et al. 2016, 2017; Tokovinin 2021).

To study multiple stellar systems, we have been performing a search for EBs utilizing the long-cadence TESS lightcurves (Kruse et al. 2022, in preparation). The lightcurves were



Original content from this work may be used under the terms of the [Creative Commons Attribution 4.0 licence](https://creativecommons.org/licenses/by/4.0/). Any further distribution of this work must maintain attribution to the author(s) and the title of the work, journal citation and DOI.

created using the *eleanor* pipeline (Feinstein et al. 2019), which uses the full-frame image (FFI) TESS data to extract photometry on a target-by-target basis. A natural by-product of this search is the identification of 97 candidates for quadruple stellar systems based on the presence of (at least) two sets of eclipses following two distinct periods and/or measured eclipse-timing variations (ETVs). These eclipses indicate quadruple candidates with a 2+2 hierarchical configuration. As part of this effort, we have already discovered the first sextuply eclipsing sextuple system (TIC 168789840, Powell et al. 2021), a compact and coplanar quadruply eclipsing quadruple system (TIC 454140642, Kostov et al. 2021b), and a transiting circumbinary planet (TIC 172900988, Kostov et al. 2021a).

Multiply eclipsing stellar quadruples are highly valuable as they provide precise measurements of orbital periods, relative stellar sizes, temperatures, and orbital inclinations—yet are quite rare as they require fortuitous alignment with the observer. At the time of writing there are about 150 *candidates* for such systems, many of which could be false positives caused by two unrelated binaries, and only a handful of *confirmed* systems (e.g., Zsche et al. 2019). Thus the catalog of uniformly vetted quadruple candidates presented here nearly doubles their numbers.

We note that the targets listed in this catalog are quadruple candidates that each originate from a single TESS source, that is, the two component EBs are unresolved in TESS data. The reason is that for the purposes of this work our interests are in close quadruple systems that can exhibit dynamically interesting interactions on a human timescale (months to years). Thus we deliberately exclude quadruple candidates that originate from two resolved sources in the TESS data (either within the same pixel or separated by multiple pixels) yet have parallaxes and proper motions that may be consistent within their mutual uncertainties. For example, two EBs that are located on two different point sources separated on the sky by half a TESS pixel ( $\sim 10''$ ) and are both at a distance of 200 pc have a sky-projected separation of 2000 au; if the two EBs are separated by 2 TESS pixels and the distance is 500 pc, the sky-projected separation is 20,000 au. If such EBs have the same proper motion they may indeed represent genuine, wide quadruple systems. However, even if there are significant dynamical interactions in such systems, the very long timescales are beyond the interest and scope of this work.

The organization of this paper is as follows: Section 2 provides an overview of detection methods, Section 3 outlines the vetting process, and Section 4 describes the ephemerides determination. We present the catalog and discuss the results in Section 5 and draw our conclusions in Section 6.

## 2. Detection Methods

A collaboration among NASA Goddard Space Flight Center (GSFC) Astrophysics Science Division, the MIT Kavli Institute, and seven experienced citizen scientists has arisen in order to fully exploit the TESS FFIs in search of interesting lightcurves. Although many different types of stellar systems as well as planets have been discovered in this pursuit, the aforementioned collaboration has specialized in the identification of triple and quadruple star systems. To rule out false positives due to nearby field stars or systematic effects, we evaluate the pixel-by-pixel lightcurve of the target as well as the motion of center of light during each set of detected

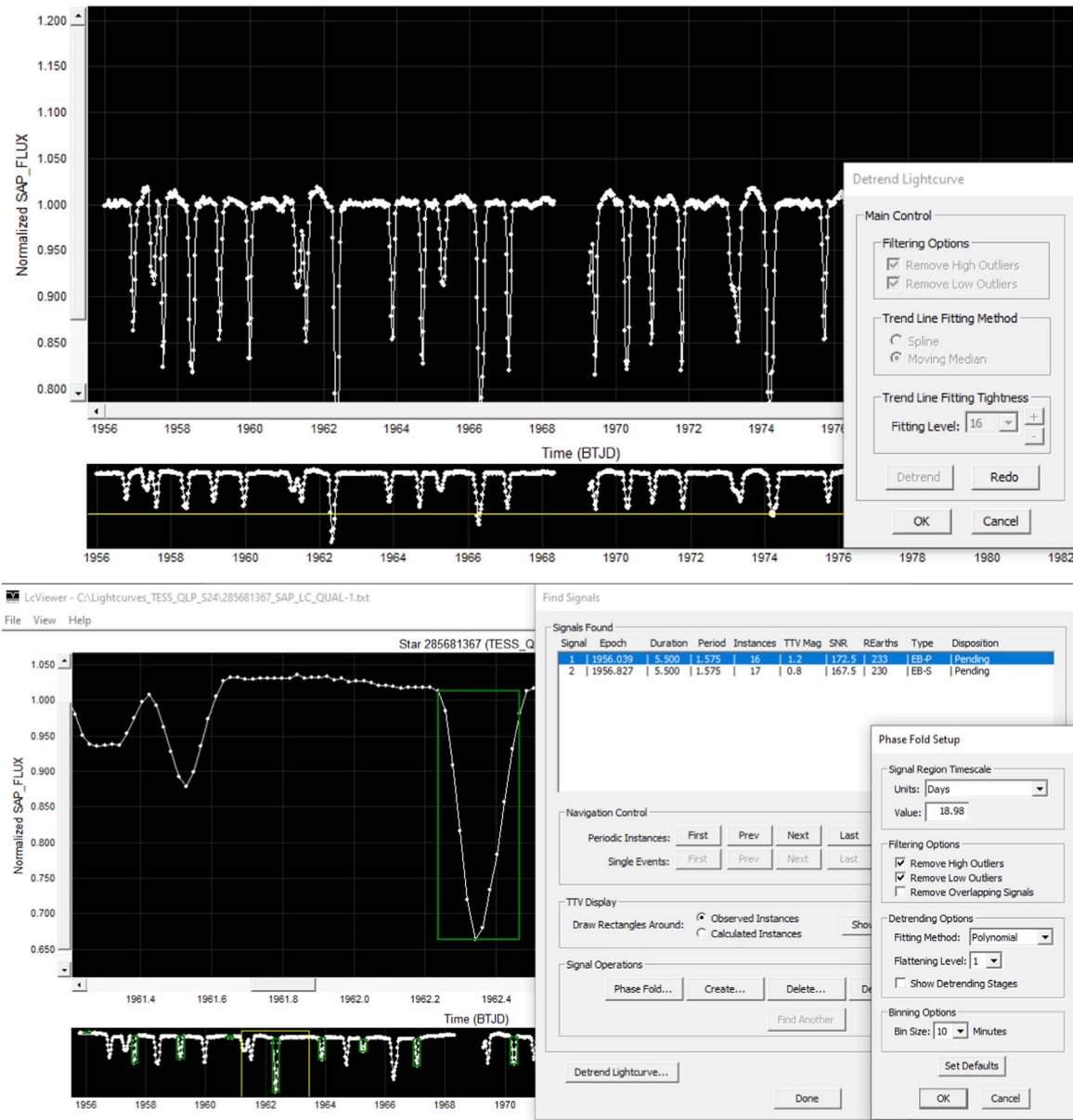
eclipses, also taking into account the stellar size and contamination ratio according to the TESS Input Catalog (TIC), as well as the astrometric noise measured by Gaia.

Following initial visual identification and inspection of the lightcurve for known artefacts, each candidate quadruple system must undergo further analysis to ensure that the eclipse signals are originating from the indicated source. Of the candidate quadruple systems identified through visual analysis, only about 5%–10% pass photocenter vetting.<sup>22</sup> The remainder are dismissed as being caused by contamination of the lightcurve by two EBs that are either physically unrelated or too widely separated on the sky (as discussed above). We note that some of these contaminated sources may actually be wide physical quadruples as per the measured parallaxes and proper motions from Gaia. Each system presented in this catalog has undergone and passed photocenter vetting, indicating, at the very least, that the source of each of the independent periods of eclipses is visually inseparable. We assess that a substantial majority of the systems presented here will be further confirmed as being gravitationally bound hierarchical quadruple systems.

Prior to this collaboration, each organization pursued these candidates through different means. The NASA GSFC group pursued machine-learning methods to find eclipses, then visually examined the lightcurves containing high-confidence eclipses. The machine-learning method is described in Powell et al. (2021). Briefly, we use a convolutional neural network adapted from the ResNet (He et al. 2015) structure to accept one-dimensional lightcurves as input. The convolutional neural network was trained to find the feature of the eclipse in the lightcurves, using over 40,000 training examples and a binary cross entropy loss function. After constructing all the FFI lightcurves from sectors 1–40 for targets brighter than 15th magnitude ( $\sim 115$  million), we used the neural network to perform inference and positively identify those lightcurves containing eclipses. Altogether, about 450,000 EB candidates were identified (E. Kruse et al. 2022, in preparation). Finally, we conducted a visual inspection of those lightcurves identified by the neural network. Given that the final step of our process was visual inspection, a collaboration with the Visual Survey Group (VSG) was natural. Since the start of our collaboration, we have continued the process of constructing the FFI lightcurves for every newly released sector of TESS data, inference through the neural network, and then a final visual survey by the VSG.

The MIT VSG (Kristiansen et al. 2022) visually examined outputs of the MIT Quick Look Pipeline (QLP; Huang et al. 2020). The VSG discoveries were all made using standard personal computers with Linux, Macintosh, or Windows operating systems. The visual surveyors made use of the LcTools software system (Schmitt et al. 2019; Schmitt & Vanderburg 2021)—an interactive set of tools designed for lightcurve analysis—and custom software written in Python, C, or JavaScript. The most common method of detection required scanning through millions of public domain lightcurves using LcTools. Where necessary, the data were detrended and filtered for additional qualification to remove systematic noise and glitches when possible. LcTools was often used to also check eclipse depth and periodicity using a built-in box-fitting least squares (BLS) or the built-in

<sup>22</sup> A catalog of quadruple false positives is beyond the scope of this work, but we plan to present such a catalog in the future.



**Figure 1.** Illustrative example of a screenshot of LcTools used to detect and analyze the quadruple candidate TIC 285681367. The upper panels show the detrended TESS QLP lightcurve of the target, along with the detrending options. The lower panels show the phase-folding setup, options, and results, as well as a zoomed-in section of the lightcurve centered on a particular eclipse used to fix the ephemeris.

QuickFind method to further qualify the candidate lightcurves. The candidates were then visually inspected for dips from possible multiple EBs. An example of this process is shown in Figure 1, highlighting the preliminary analysis of quadruple candidate TIC 285681367.

We note that trained visual inspection for *specific features* (like additional eclipses superimposed on an otherwise regular pattern) using tools specifically designed for the task can be quite fast and efficient. The three main reasons are that (1) LcViewer is extremely fast with close to zero lag time between lightcurve presentations and presents the lightcurves in a consistent, uniform, and homogeneous format; (2) the seasoned visual surveyor is experienced in knowing what an object of interest looks like as well as whether it is a known pattern or not; and (3) human perception is exceptionally good at recognizing a change in a known pattern or the emergence of

a new pattern. For example, showing a trained surveyor 99 consecutive images of trees planted at regular intervals (like eclipses) is unlikely to trigger a reaction if asked to identify a new pattern. While the types of trees and the intervals change between images, the size, shape, and color pattern of the images remain the same so that, in essence, the trees (eclipses) practically *become* the background. If, however, the 100th image contains a tiger hiding behind a new set of trees planted at a regular interval, the surveyor will raise a red flag in a matter of seconds.

From our experience with Kepler, K2, and TESS data, members of our team can inspect a particular lightcurve in about 5–10 s, and potentially much faster. Thus assuming a typical “cruising speed” of 10 s per lightcurve, 10 dedicated visual surveyors can inspect 1 million lightcurves in 2 years spending less than 25 minutes a day. For context, over the last



10 yr VSG members have visually surveyed more than 15 million lightcurves from Kepler, K2, and TESS (Kristiansen et al. 2022). In comparison, the subsequent vetting process (described below) is orders of magnitude slower.

### 3. Vetting Methods

Due to the large pixel size of the TESS photometer ( $\approx 20''$ ), false positives due to nearby field stars are a common occurrence. To account for this, we evaluate the motion of the measured center of light during each set of eclipses detected in the lightcurve of each target. We also take into account the presence of nearby field stars and their respective magnitude differences with the target star, contamination ratio according to the TIC where available, and information from the Gaia EDR3 catalog. In addition, we pursue follow-up photometry observations for a subset of targets as part of the TESS Follow-up Observing Program, as well as dedicated spectroscopy on the 1.5 m telescope at the F. L. Whipple Observatory in Arizona with the Tillinghast Reflector Echelle Spectrograph (TRES; Szentgyorgyi & Fűrész 2007; Fűrész 2008).

The vast majority of our quadruple candidates were unknown as EBs prior to their detection with TESS. As a result, they were not on the list of TESS targets observed at 2 minutes' cadence and no data validation reports were available. Thus we used a center-of-light analysis based on the photocenter module of the DAVE vetting pipeline (Kostov et al. 2019) to evaluate the source of the detected EBs. Briefly, we investigate the center-of-light motion for each eclipse of each EB for each sector of available data by fitting to the difference image (out-of-eclipse image minus in-eclipse image) a point-spread function and a pixel-response function and measuring the corresponding photocenter. When the eclipses of two EBs are too close to each other in time, so that there is little to no out-of-eclipse section of the lightcurve available for photocenter measurement, we exclude said eclipses from the analysis. To evaluate whether there is a significant motion during the detected eclipses, we compare the measured average difference image photocenter to the pixel position of the target as provided in the corresponding FITS header. We note that comparing the photocenter measured from the average difference image to the photocenter measured from the average out-of-eclipse image, as used for the analysis of Kepler and K2 data, is not optimal for TESS. The reason for this difference is that the TESS aperture is much larger and often contains multiple field stars that are as bright as the target itself (or even brighter). As a result, these field stars “pull” the measured out-of-eclipse photocenters away from the position of the target star, effectively preventing a meaningful comparison between the difference image and the out-of-eclipse image. While this was a known issue for K2 data (e.g., Kostov et al. 2019), it is much more prevalent for TESS data.

Based on our experience, the resolution limit of the photocenter analysis depends on multiple factors, which typically vary not only on a target-by-target but also on a sector-by-sector basis. Specifically, the limiting factors are the (1) magnitude difference between the target and nearby field stars; (2) overall contamination ratio; (3) out-of-eclipse lightcurve variability; (4) number and depth of clean, unblended eclipses; (5) quality of the difference images used to measure the photocenters; and (6) peculiarities of the systematic effects. For a typical pair of sources, measuring a photocenter separation of  $\sim 5''$ – $10''$  ( $\sim 0.25$ – $0.5$  pixels) is relatively easy, whereas a separation of  $\sim 1''$  ( $\sim 0.05$  pixels) is highly challenging.

We note that for some targets the TIC and/or Gaia EDR3 catalogs show that there is indeed a field star within  $\sim 1''$  of the target, and the photocenter measurements may not be sufficiently precise to pinpoint the true source of the eclipses. In these cases, we evaluate whether the eclipses can be produced by a field star using the eclipse depth ( $d_e$ ) and the magnitude difference in the TESS bandpass ( $\Delta T$ ) between the field star and the target star,  $\Delta T = -2.5 \log_{10}(2d_e)$  mag. For example, for a field star to produce 10%-deep eclipses as contamination in the target's TESS lightcurve,  $\Delta T$  has to be smaller than about 1.75 mag.

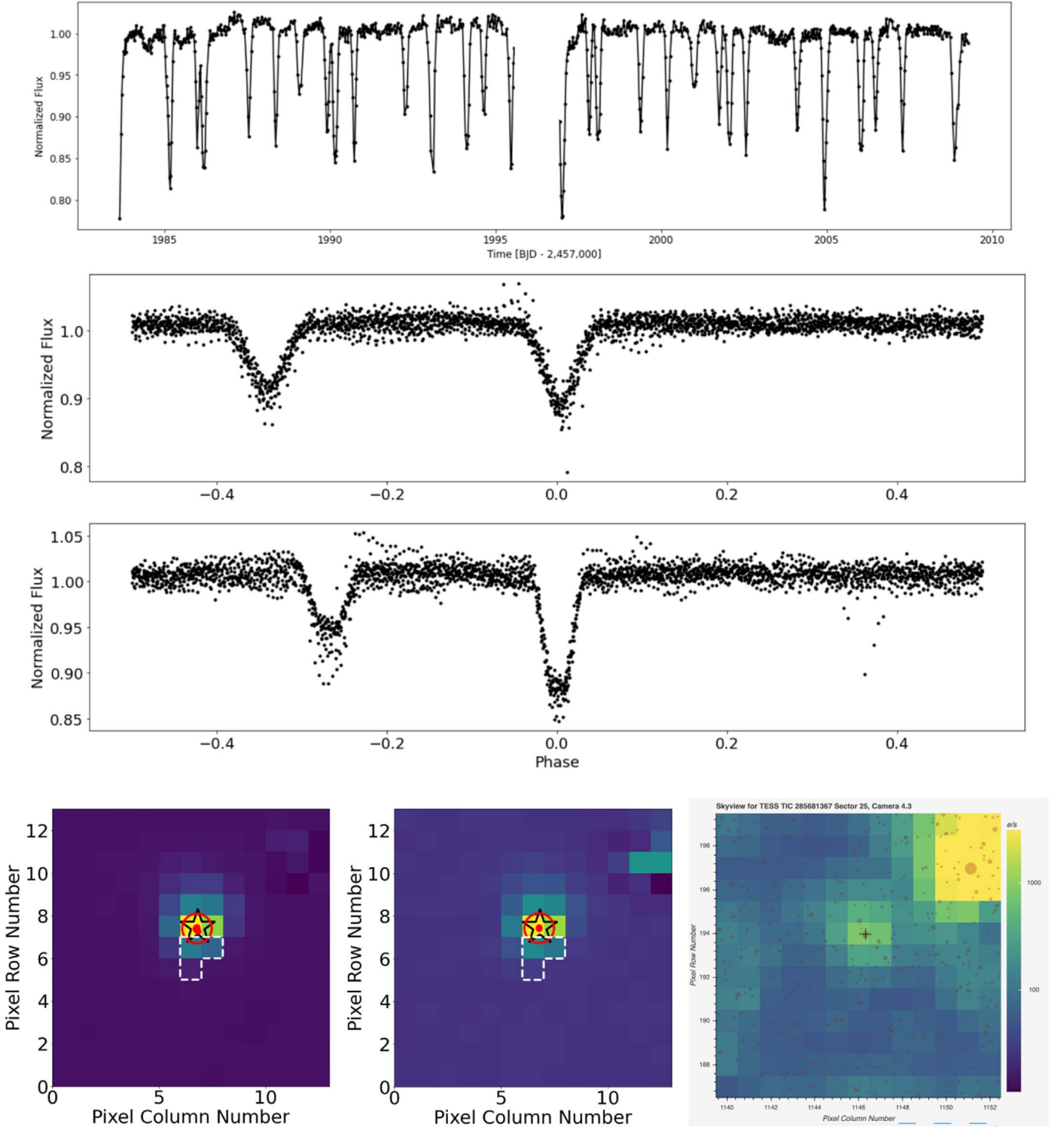
An example of a quadruple candidate (TIC 285681367) passing these vetting tests is shown in Figure 2. The target was observed in sectors 18, 24, and 25 and produced two sets of eclipses with periods of  $P_A = 2.3660$  days and  $P_B = 3.9703$  days, each showing primary and secondary eclipses. The FFI lightcurve of the target for sector 25 is shown in the upper panel of the figure. The lower left and middle panels of the figure show the average difference images for each set of primary eclipses; the red symbols represent the measured photocenters, and the black star represents the catalog position of the target. Our photocenter analysis shows that the target is the source of both sets of eclipses. We note that the aperture *eleanor* used for TIC 285681367 in sector 25 (dashed contour in lower left and middle panels) does not include the target itself. This is a relatively rare (and sector-dependent) occurrence and indicates that the eclipses are actually deeper than what we see in the *eleanor* lightcurve.

Throughout this work, we used *eleanor*'s default *aperture\_mode* = “normal” option, which, by design, already tests various aperture sizes depending on the target's magnitude and contamination ratio. Further adjusting the photometric aperture in order to extract a custom lightcurve would require modifying the source code itself. This is beyond the scope of our work and would likely require working closely with the creators of *eleanor*. However, the aperture only affects the measured eclipse depths. It does not affect our photocenter analysis at all because we use our own codes and all available pixels as directly provided by TESS (typically a  $13 \times 13$  pixel cutout; see lower left panel in Figure 2).

The lower right panel of Figure 2 represents a Skyview image of the target's TESS aperture (with the same size as the difference images,  $13 \times 13$  pixels) showing all stars down to  $G = 21$  mag. This is a crowded field—the target is blended with TIC 627730721 (separation  $\approx 2''.7$ ,  $\Delta T \approx 7.3$  mag), and there are two more field stars inside the central pixel for sector 25—TIC 627730803 (separation  $\approx 5''.1$ ,  $\Delta T \approx 7.3$  mag) and TIC 627730804 (separation  $\approx 6''.5$ ,  $\Delta T \approx 8.6$  mag). However, none of these field stars is bright enough to produce the detected eclipses.

#### 3.1. Pixel-by-pixel Analysis

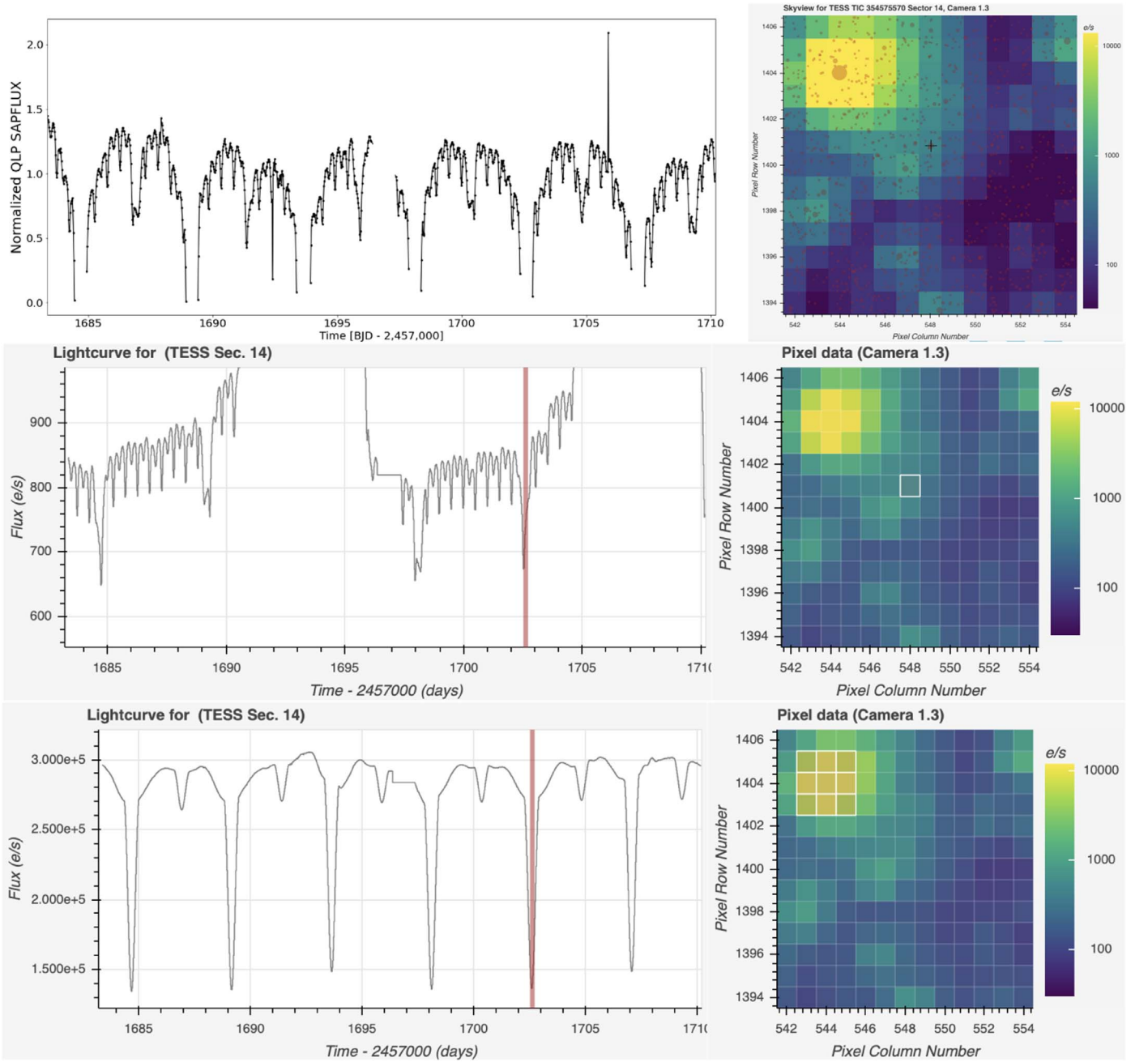
Once a multistellar candidate is identified, we utilize the interactive feature in Lightkurve (Lightkurve Collaboration et al. 2018) to inspect the target pixel file as an initial test prior to the photocenter analysis discussed above. As a standard, we compute a  $15 \times 15$  pixel cutout, which normally encompasses both EBs in question. The size of the cutout is based on a compromise between reliability and efficiency. In terms of reliability, our experience shows that this pixel mask allows consistent identification of the location of both EBs, regardless of their brightness. In terms



**Figure 2.** Upper panel: long-cadence TESS *eleanor* lightcurve of TIC 285681367, showing two sets of eclipses with period  $P_A = 2.37$  days and  $P_B = 3.97$  days. Second and third panels from top: phase-folded lightcurve for binary A and binary B, respectively. For clarity, the lightcurve was disentangled such that the eclipses of the other binary were removed (Powell et al. 2021). Lower left and middle panels: TESS difference images ( $13 \times 13$  pixels) for  $P_A$  and  $P_B$ , respectively, showing the pixels changing during the corresponding primary eclipses. The axes represent the corresponding relative pixel number along the  $x$ -axis (pixel column number) and  $y$ -axis (pixel row number). The small red symbols represent the measured photocenter for the individual primary eclipses of each respective binary, and the large red circle shows the corresponding average photocenters. The black star is the catalog position of the target, and the dashed contour represents *eleanor*'s aperture used to extract the target's FFI lightcurve. Lower right panel: Skyview image (also  $13 \times 13$  pixels) of the target's TESS aperture showing known nearby sources down to  $G = 21$  mag. The photocenter analysis shows that both sets of eclipses are on target.

of efficiency, the computational time is negligible compared with the time needed to adjust the aperture in an attempt to find the perfect match for each target. We also note that a

contaminating star does not need to be exceptionally bright—only bright enough compared with the target star itself (see Section 3 for details).



**Figure 3.** Example quadruple false positive for scenario (1) described in Section 3.1. First row, left panel: sector 14 QLP lightcurve of TIC 354575570 as used by the visual surveyors for the detection of two apparent sets of eclipses. First row, right panel:  $15 \times 15$  pixels Skyview image of the target’s TESS aperture showing known nearby sources. Middle and lower rows: Lightcurve visualization of the selected pixels (white contours in right panels) and the corresponding lightcurve (left panels). The target is a quadruple false positive as one of the EBs is clearly off target.

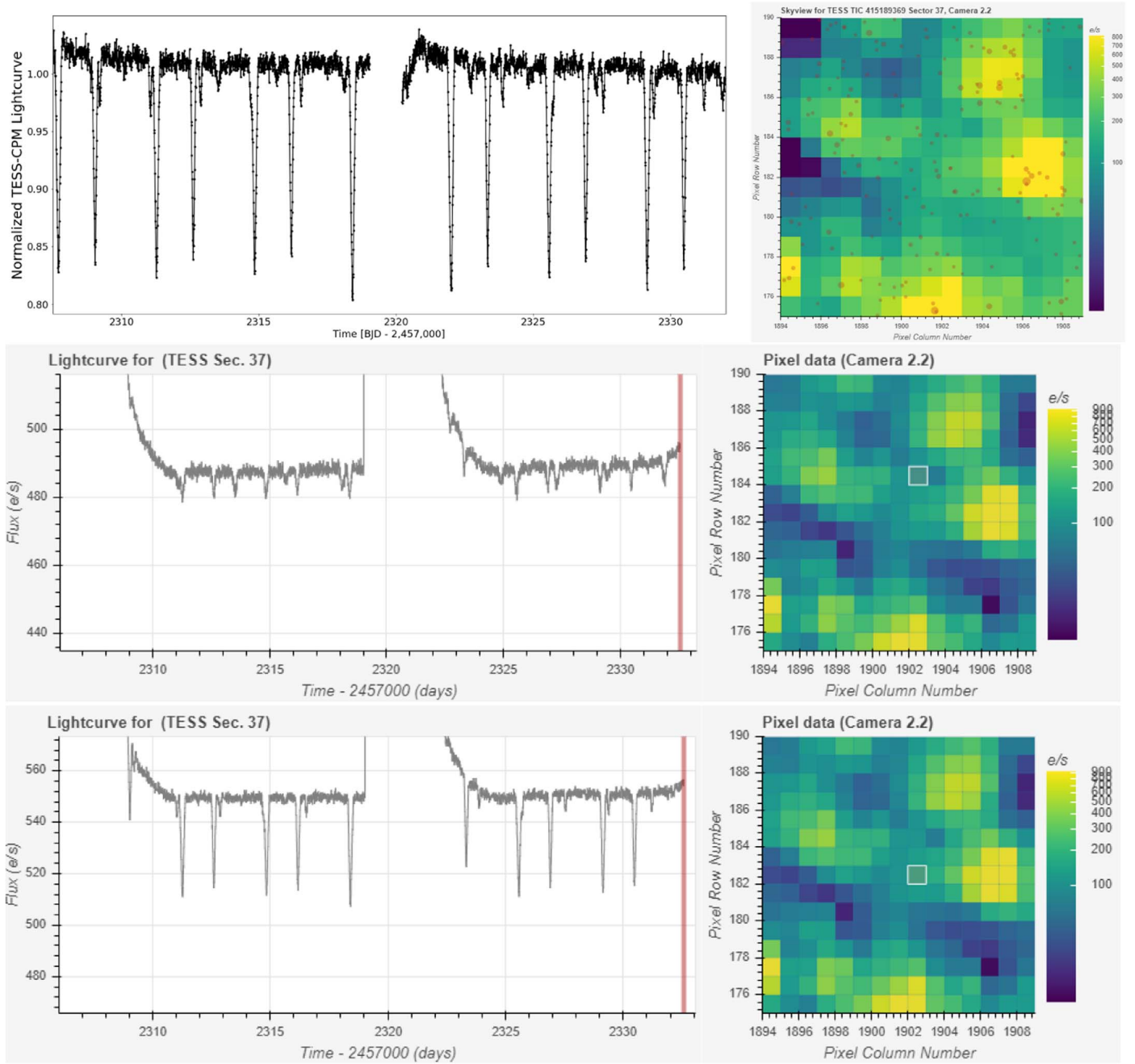
In most cases, we experience one of the following scenarios: (1) the two EBs are sufficiently separated on the sky with at least one EB being off target; or (2) the positions of the two EBs are in adjacent pixels (as inferred with *Lightcurve*), yet different apertures show that the corresponding eclipse depths scale differently as a function of the aperture size. This indicates that the EBs originate from two resolved targets, which may or may not be a wide quadruple system. These two scenarios can be further evaluated by comparing parallax and proper motion values, which we find via the Swarthmore Finding Chart through ExoFOP-TESS. Examples of these scenarios are shown in Figures 3 and 4.

We note that there can be more than two unrelated stars in a target’s TESS aperture (i.e., with different Gaia distances and/or proper motions), coming from clearly distinct pixels of the aperture. For example, there are four unrelated EBs in the TESS aperture of quadruple false-positive TIC 28553336. Finally, sometimes two or more stars are located very close to each other within the same pixel. In cases like this, pinpointing the source of each EB needs further analysis as discussed above.

### 3.2. Types of False Positives

All candidate quadruples listed in this catalog have passed the photocenter vetting process described above. Those that did





**Figure 4.** Same as Figure 3 but for false-positive scenario (2). First row, left panel: TESS-CPM lightcurve for TIC 415189369 (Hattori et al. 2020). The target is a quadruple false positive as the relative depths of the two sets of eclipses scale differently depending on the selected pixel. Middle and lower rows: Lightcurve visualization of the selected pixels (white contours in right panels) and the corresponding lightcurve (left panels).

not pass the process fall into several categories, described below for completeness.

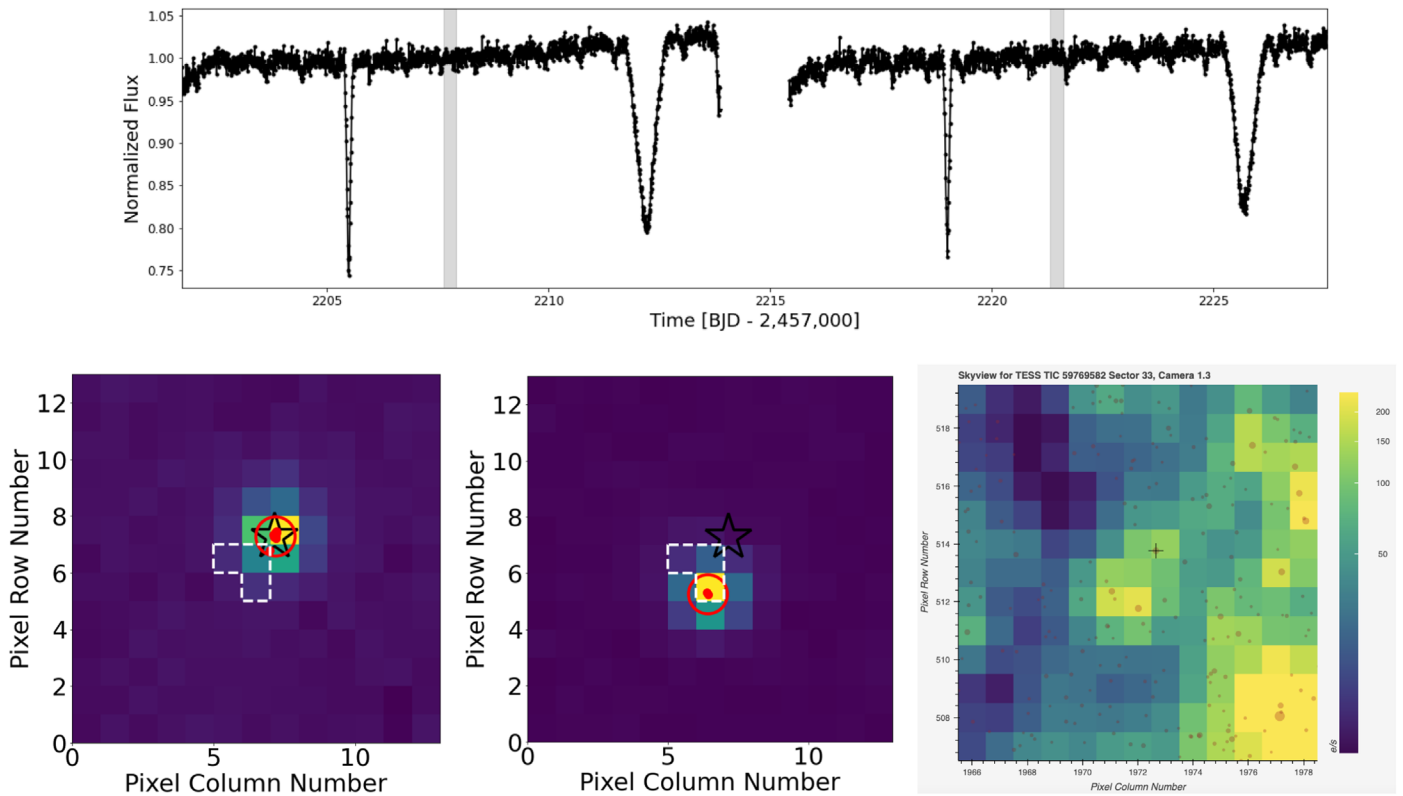
In general, we encountered the following five false-positive scenarios:

1. Target EB + field EB: A scenario where the photometer analysis shows that one of the detected EBs is the target itself and the other is a nearby field star whose signal bleeds into the target's aperture (see Figure 5).
2. Field EB (star 1) + field EB (star 1): A scenario where the photometer analysis shows that both EBs originate from a nearby quadruple candidate that bleeds into the aperture of the target star (see Figure 6). We note that here the

off-target quadruple is a genuine candidate, but the target itself is considered in this work to be a false positive.

3. Field EB (star 1) + field EB (star 2): A scenario where the photometer analysis shows that two EBs from two field stars bleed into the target's aperture (see Figure 7). Star 1 and star 2 may or may not be in a wide quadruple system.
4. Target triple star: A scenario where a triply eclipsing triple star produces a single pair of tertiary eclipses that mimic a second highly eccentric EB with a period longer than the duration of the observations; the photometer analysis shows that tertiary eclipses originate from the target. If there are more pairs of these eclipses in additional sectors of data, the target can be immediately marked as a triply





**Figure 5.** Long-cadence TESS *eleanor* lightcurve (upper panel) and photometer analysis (lower left and middle panels) of TIC 59769582. The analysis shows that binary A with  $P_A = 1.57$  days is on target (lower left panel), while binary B with  $P_B = 13.5$  days is off target (lower middle panel), about 2 pixels SW of TIC 59769582. The lower right panel shows the Skyview image of the TESS aperture for TIC 59769582 (at the center of the image, marked with a plus symbol), highlighting the source of the  $P_B$  eclipses (red arrow). This is an example of on-target EB + field star EB false positive.

eclipsing triple star as the pairs of tertiary eclipses will (usually) vary in shape and order between consecutive conjunctions (see Figure 8)

5. Potential false positive: A case where one or more field stars nearly overlap with the target and are bright enough to produce a second set of eclipses in the target’s lightcurve. The angular separation between the target and the field stars (subarcsec separation) is too small for reliable photometer measurements and is likely beyond the capabilities of dedicated follow-up as well (see Figure 9). The contaminating field star may or may not form a physical quadruple with the target.

#### 4. Ephemeris Determination

To determine the ephemerides of the two EBs for each quadruple candidate in this catalog, we perform the following steps. First, we run a preliminary BLS (Kovács et al. 2002) analysis of the lightcurve of each target for each available sector. Where needed, we clean the lightcurve by removing sections with partially or fully blended eclipses, as well as sections exhibiting known systematic effects. Additionally, for targets exhibiting prominent out-of-eclipse modulations we detrend the lightcurve by masking out the eclipses, applying a Savitsky-Golay filter to remove the variability, and adding the eclipses back in. For completeness, we include in our catalog relevant comments for any targets exhibiting prominent lightcurve variability due to either potential ellipsoidal modulations or general variability (e.g., TIC 271186951, TIC 357810643, TIC 367448265). Next we extract small sections of the lightcurve centered on each eclipse for each binary, with a typical length of

two to three eclipse durations as measured by BLS. Finally, using these sections we measure the eclipse times, depths, and durations using four different functions—a trapezoid, a Gaussian, a generalized Gaussian of the form

$$F(t) = A - Be^{-\left(\frac{|t-t_o|}{\omega}\right)^\beta} + C(t - t_o), \quad (1)$$

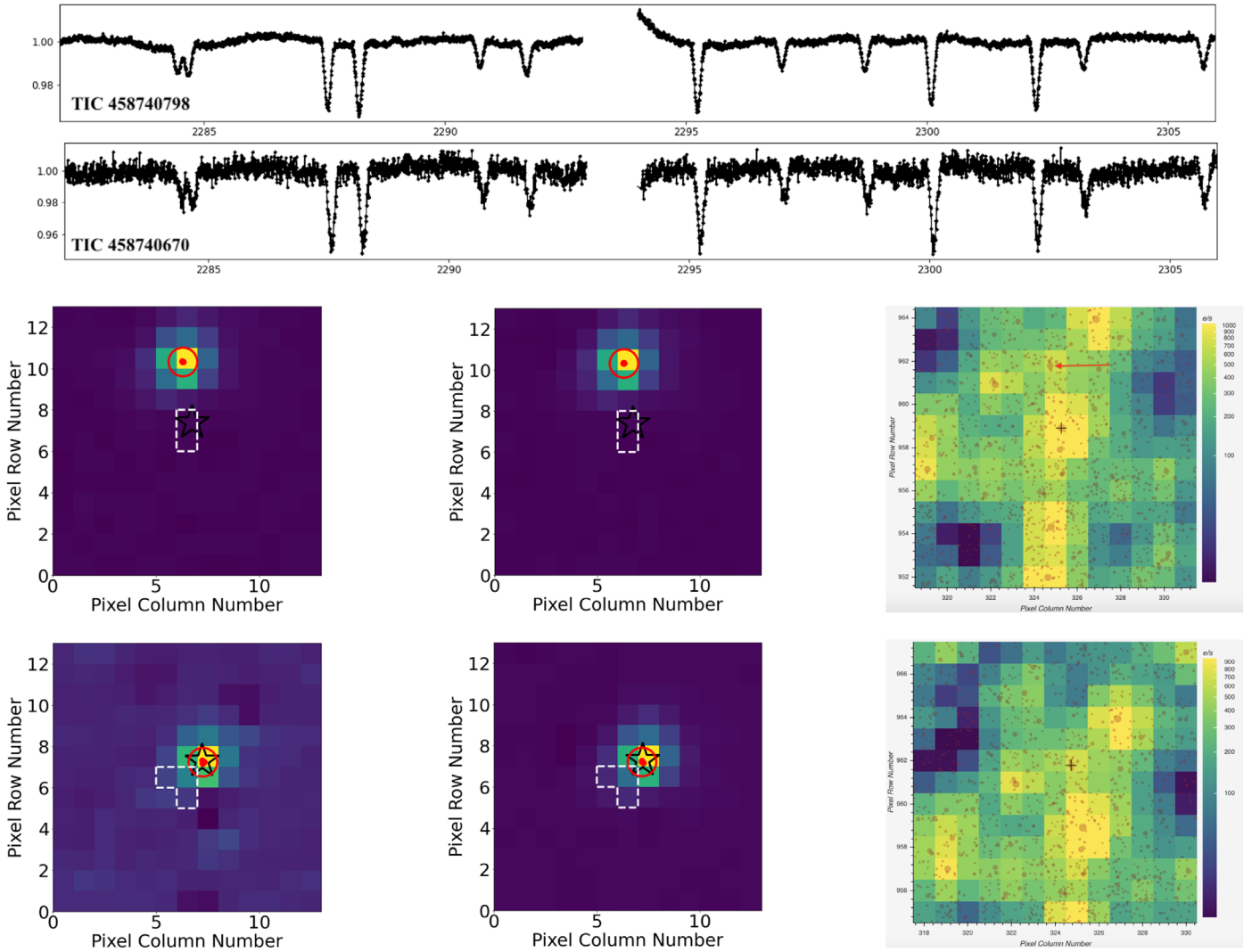
and a generalized hyperbolic secant of the form

$$F(t) = A - \frac{2B}{e^{-\left(\frac{|t-t_o|}{\omega}\right)^\beta} + e^{\left(\frac{|t-t_o|}{\omega}\right)^\beta}} + C(t - t_o), \quad (2)$$

where  $A$ ,  $B$ ,  $C$ ,  $t_o$ ,  $\omega$ , and  $\beta$  are free parameters. For  $\beta=2$ , Equation (1) becomes a standard Gaussian except for an additional factor of 2 in the denominator of the exponential (which can be absorbed into  $\omega$ ). We note that (1)  $\beta$  can take noninteger values and (2) the  $C(t - t_o)$  term in Equations (1) and (2) helps minimize the effects of in-eclipse lightcurve variability by accounting for a residual linear trend.

Because eclipse depths can vary between sectors (due to genuine changes caused by dynamical interactions or simply because of systematics), we fit each eclipse individually and then adopt the measurements from the corresponding function that provides the smallest chi-square. An example is shown in Figure 10 for the case of TIC 392229331. Here, although the four functions look similar to the eye, the generalized Gaussian provides the best fit: the chi-square ratios between the generalized Gaussian function and the Gaussian, generalized hyperbolic secant, and trapezoid are  $\approx 0.77$ ,  $0.84$ , and  $0.95$ , respectively.

The differences between the Gaussian and the generalized Gaussian and secant functions—and the benefit of using the



**Figure 6.** An example of a nominal false positive (TIC 458740798) caused by a genuine quadruple candidate (TIC 458740670) in the field. First row: long-cadence TESS *eleanor* lightcurve of TIC 458740798 for sector 36 (the false positive). Second row: same as first row but for TIC 458740670 (the quadruple). Note how all eclipses are deeper on TIC 458740670, already indicating that it is the source of the eclipses. Third row, left and middle panels: photocenter analysis for TIC 458740798, showing the difference images (left for binary A with  $P = 6.26$  days, middle for binary B with  $P = 7.02$  days), along with the pixel-response function-based measurements of the individual photocenters (small red dots) and average photocenter (large open circle). The black star symbol indicates the catalog position of TIC 458740798. The measured photocenters are centered on a location about 3 pixels above TIC 458740798—near the position of TIC 458740670. Third row, right panel: Skyview image of the TESS aperture for TIC 458740798 (at the center of the image, marked with a black plus symbol), highlighting the true source of the eclipses TIC 458740670 (red arrow). Fourth row: same as third row but for TIC 458740670—a genuine quadruple candidate—showing that the measured photocenters coincide with the location of TIC 458740670. Note that *eleanor*’s aperture for TIC 458740670 is adjacent to the target, and as a result the true eclipse depths are larger than those seen in the lightcurve (second row).

latter two—become more pronounced the flatter/sharper the eclipse bottom is. This is highlighted in Figure 11 for the primary eclipses of binary B of TIC 285681367 (see also Figure 2). Here the eclipse shape clearly deviates from a Gaussian but is well represented by the generalized Gaussian and secant functions (as well as the trapezoid function).

This approach allows us to keep track of potential eclipse-time variations that might indicate dynamical interactions between the two EBs. Indeed, several systems exhibit such variations as discussed below.

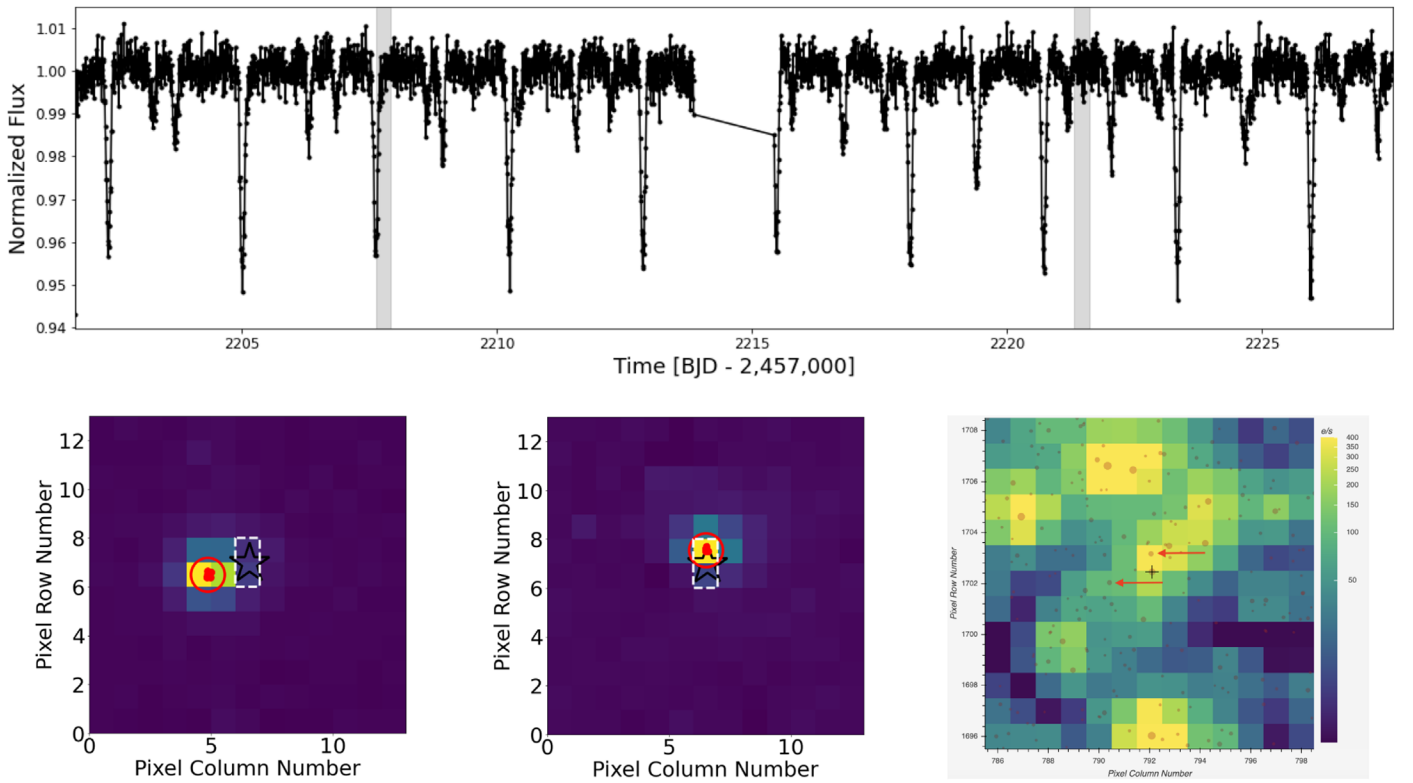
## 5. The Catalog

### 5.1. Contents of the Catalog

The catalog presents the TIC ID, periods, eclipse times, depths, durations, and secondary phases of the potential quadruple

systems detected in the GSFC FFI lightcurves (B. Powell et al. 2022, in preparation, E. Kruse et al. 2022, in preparation), as well as additional comments including important features, issues, caveats, etc. The results are summarized in Table 1. For completeness, the table also provides the estimated composite effective temperature and the TESS magnitude from the TIC, as well as the Gaia EDR3 distance and identifier; for convenience, we label the targets as, for example, TGV-1 for “TESS/Goddard/VSG quadruple candidate-1.”

The sky coordinates of the 97 quadruple candidates are shown in Figure 12. Compared with the quadruple candidates listed in Zasche et al. (2019), our targets are uniformly spread in decl. (see their Figure 12 versus the upper right panel of Figure 12 here). The apparent lack of targets in some parts of the sky (e.g., southern targets with R.A. greater than about  $250^\circ$ ) is likely due to the incompleteness of our catalog—there



**Figure 7.** Same as Figure 5 but for TIC 262535168. The two EBs seen in the lightcurve originate from two different targets, neither of which is TIC 262535168, as highlighted on the Skyview image. This is an example of a false positive due to field EB (star 1) + field EB (star 2).

are many more potential quadruple candidates in our database awaiting vetting and analysis.

A powerful tool to infer the potential presence of unresolved companion(s) in a given stellar system is measurements of astrometric noise in excess of that expected from the target's parallax and proper motion. The Gaia EDR3 catalog (Gaia Collaboration et al. 2021) provides such measurements in terms of an astrometric excess noise above a single star model, that is, AEN, with a corresponding significance AENS, as well as an indicator for the astrometric goodness of fit in terms of an RUWE. The method has been demonstrated for known spectroscopic binaries, which are used to measure binarity fraction across the Hertzsprung–Russell diagram and detect hierarchical triples and X-ray binary stars (e.g., Belokurov et al. 2020; Penoyre et al. 2020; Stassun & Torres 2021; Gandhi et al. 2022, and references therein). Figure 12 shows Gaia's EDR3 AEN, AENS, and RUWE for those targets in our catalog with measured AEN (91 out of 97). Of these 93, the AEN is greater than 1/5/10 mas for 32/7/6 targets and can reach up to 93 mas (for TIC 168789840). Most of the targets (90) have AENS greater than 5, and 56 targets have AENS > 100; more than half of the targets (59 out of 91) have RUWE greater than 1.5 (the value above which the astrometry is likely affected by wide companions) and 20 targets have RUWE greater than 10. Altogether, these indicate potentially significant orbital motion between the two unresolved components for a large number of the quadruple candidates presented in this catalog.

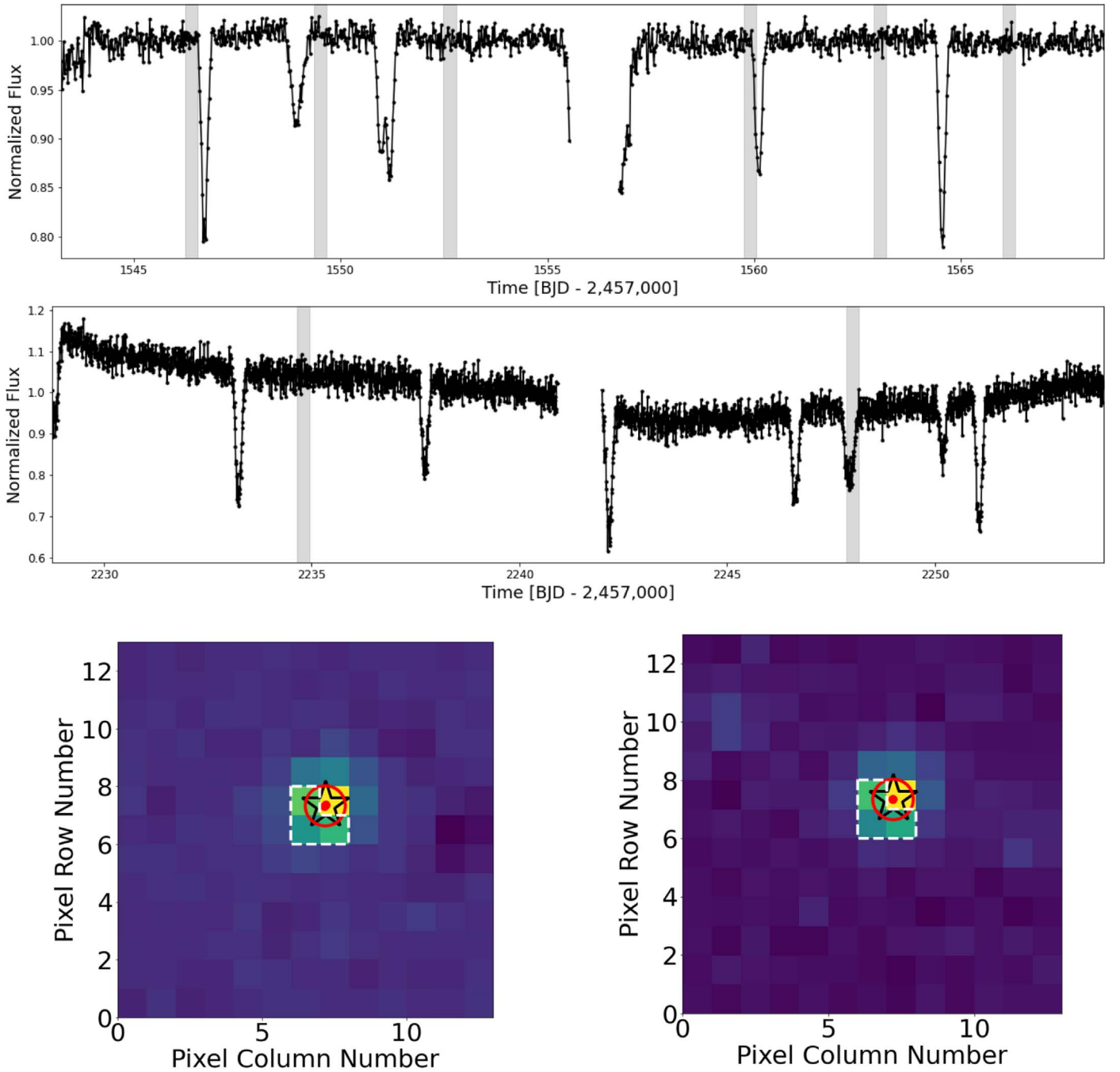
### 5.2. Period Distributions

Recent analysis of quadruple systems consisting of two EBs in a 2+2 hierarchical configuration shows strong peaks near period ratios of 1/1 and 3/2, a smaller peak near 5/2, and no

significant peak near 2/1 (Zasche et al. 2019). The systems representing the 1/1 peak are close to resonance but not exactly in resonance, and only about a quarter of the systems representing the 3/2 peak are close to an exact period ratio. With the caveat that some of the studied systems may not be genuine quadruples, and also assuming coplanar orbits, it has been suggested that period ratios of 2/1 and 3/2 could be due to resonant capture and should be common (Tremaine 2020). However, a period ratio near or at 1/1 is expected to be rare as the corresponding resonance capture is inefficient (Breiter & Vokrouhlický 2018; Tremaine 2020). This makes the origin of the 1/1 peak in the Zasche et al. (2019) sample puzzling.

Our catalog of uniformly vetted quadruple candidates presents a new opportunity to study period distributions. These are shown in Figure 13 for the 97 candidates that pass our vetting tests measurements. As a comparison to Figure 13 of Zasche et al. (2019), 72 of the 97 systems have period ratios  $P_B/P_A$  smaller than 4. The distribution of these 72 systems is shown as a histogram in the upper right panel of Figure 13 presented here, using the same number of bins as Zasche et al. (2019) (26). Of these 72 systems, 24 (7) have period ratios of 1:1, 5:4, 4:3, 3:2, 5:3, 2:1, 5:2, and 3:1 to within 4% (1%), respectively; the value of 4% was chosen as twice the difference between the 5:4 and 4:3 period ratios.

To evaluate the significance of the measured period ratios, we computed the matches to rational numbers 1:1, 5:4, 4:3, 3:2, 5:3, 2:1, 5:2, and 3:1 to within 8%, 4%, 2%, and 1% for a simulated distribution of period ratios as follows. First, we selected  $P_A$  periods measured randomly according to a  $dp/dP_A \propto P_A^{-1}$  probability distribution covering the range of 0.3–16 days (in line with the 72 systems outlined above). Next, for any given  $P_A$  we selected  $P_B$  randomly according to



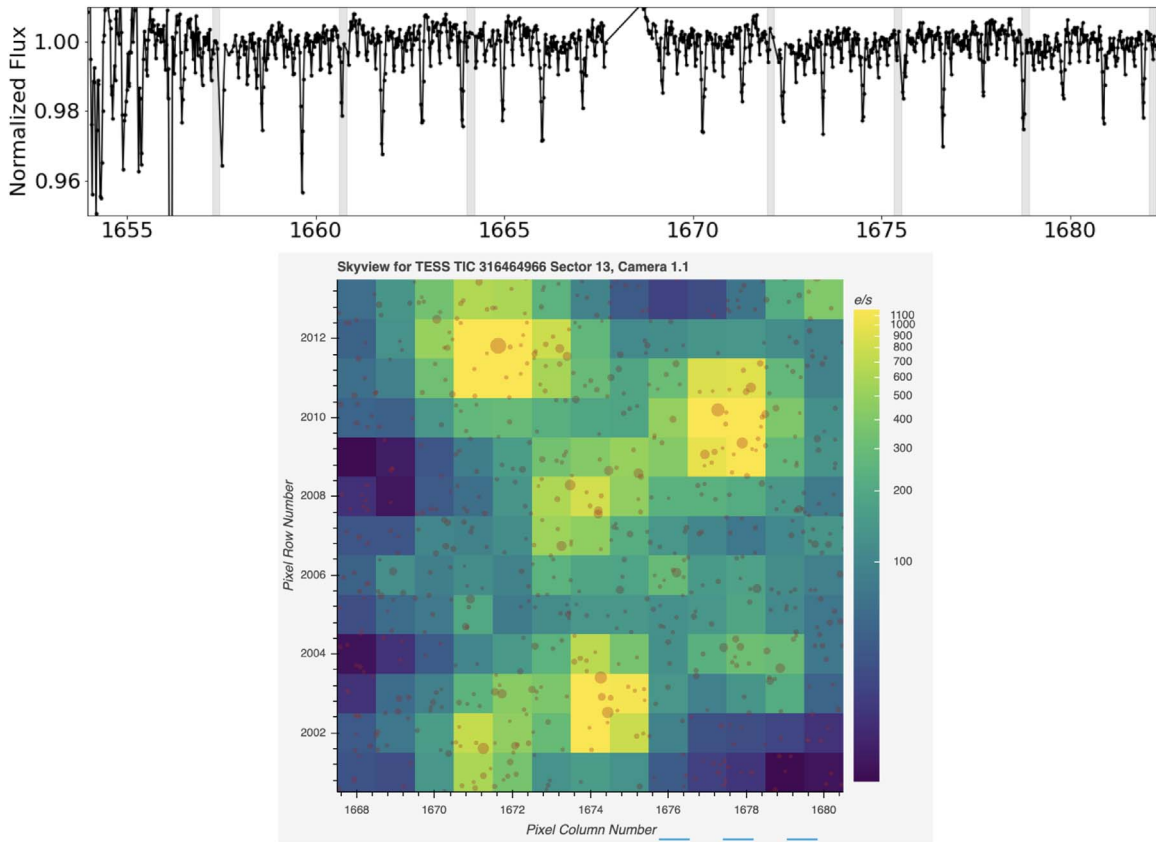
**Figure 8.** First and second row: long-cadence TESS *eleanor* lightcurve of TIC 53201931, a triply eclipsing triple star producing a pair of tertiary ellipses in sector 9 (first row, 30 minutes cadence) and in sector 34 (second row, 10 minutes cadence). Third row, left and right panels: photocenter measurements for the inner binary (left, with a period of 8.9 days) and for the third star (right, with a period that is  $\sim 700/N$ , where  $N$  is an integer). Note how the pair of tertiary eclipses change shape and order—the “smoking gun” signature of a third star orbiting the EB. This is an example of on-target false-positive quadruple due to a triple star.

$dp/dP_B \propto P_B^{-4/3}$  such that  $P_B$  ranges from  $P_A$  to 25 days; we experimented with various empirical power-law indices and found that the value of  $4/3$  yielded approximately the observed fraction of systems with  $P_B/P_A (<4)$  versus with  $P_B/P_A (>4)$ . This was done 72 times to make a complete simulation of one TESS data set. For each simulated period ratio we checked whether this ratio was within a certain percentage of a rational number. We then stored the number of matches within the set of 72 ratios. Finally, the entire process was repeated  $10^5$  times and distributions of matches to rational numbers were

computed. The mean numbers of expected matches versus those found in the data, as a function of the percentage match requirement, are listed in Table 3.

Overall, these simulations show that the numbers of accidental matches with rational numbers agrees to within the statistical uncertainties with the observed numbers for each of the four percentage match requirements. From this, we conclude that there is no evidence in our data set for an enhancement of period ratios in quadruples at the rational number values. In turn, this indicates that either (1) we have





**Figure 9.** Upper panel: long-cadence TESS *eleonor* lightcurve of PTIC 316464966 showing two sets of eclipses, with periods of  $P_1 = 1.06$  days and  $P_2 = 0.24$  days. The TIC lists two stars separated by about  $1''.11$ , TIC 1821336783 and TIC 1821336772, with respective magnitudes of  $T = 13.83$  mag and  $T = 14.27$  mag. Either star can produce either set of eclipses, and the separation between them is too small for reliable photocenter measurements. This is an example of a potential false positive due to blended stars that are too far apart to be of interest for this study (in this case  $\sim 1000$  au).

insufficient statistics to conclude that there is an enhancement at rational number period ratios or (2), if nature prefers special period ratios, they are not sufficiently close to rational numbers for us to measure them.

Finally, once the quadruple orbital period and eccentricity are known, a dynamical stability study on these systems would provide further proof that they are not just coincident but gravitationally bound.

### 5.3. Secondary Eclipses, Eclipse Depth, and Duration Distributions

The phase difference between primary and secondary eclipses directly constrains  $e \cos(\omega)$ . As the eclipse times can be measured reasonably well from the data, even at relatively low signal-to-noise ratio (S/N),  $e \cos(\omega)$  can be readily estimated. The other component of the orbital eccentricity,  $e \sin(\omega)$ , is constrained by the difference between the primary and secondary eclipse durations (e.g., Prsa et al. 2011). The eclipse durations are more difficult to measure compared with the eclipse times, and thus  $e \sin(\omega)$  is less well constrained. With this in mind, the distributions of the measured  $e \cos(\omega)$  and  $e \sin(\omega)$  for the quadruple candidates presented in this catalog are shown in Figure 14. Both distributions are strongly clustered around 0.0, suggesting a tendency for circular orbits. Given the relatively short orbital periods ( $< 15$ – $25$  days, see Figure 13), this is not unexpected. The measured duration ratios between the primary and secondary eclipses are smaller

than 1.5, with the exception of TIC 1337279468, binary C, where it is  $\approx 4$ .

We note that the individual eclipse depths reported in Table 1 are guaranteed to be different from the true depths due to the mandatory “contamination” produced by the contribution of the other binary to the total light of each A + B system. However, the ratio between the primary and secondary eclipse depths—an indicator of the relative brightness of the two stars in each binary, as well as of the orbital eccentricity—is less affected by said contamination. The measured eclipse depth ratios are presented in Figure 14, showing no clear preference toward a specific value.

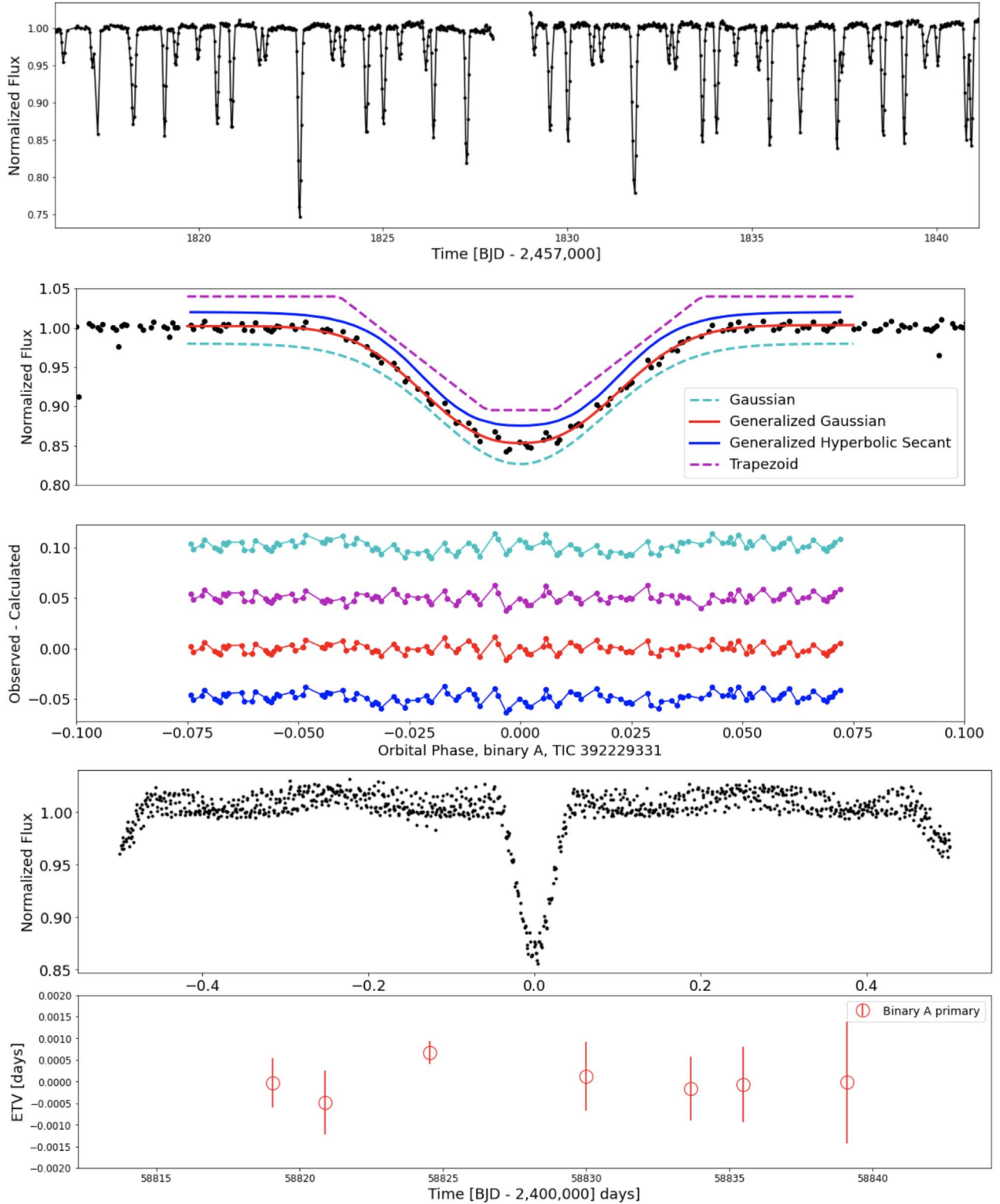
### 5.4. Discussion

A uniformly vetted catalog of eclipsing quadruple systems provides the opportunity to examine in further detail both individual systems of particular interest, as well as study broader questions relevant to their formation and evolution.

#### 5.4.1. Individual Systems

Below we list several potentially interesting systems detected as part of this work.

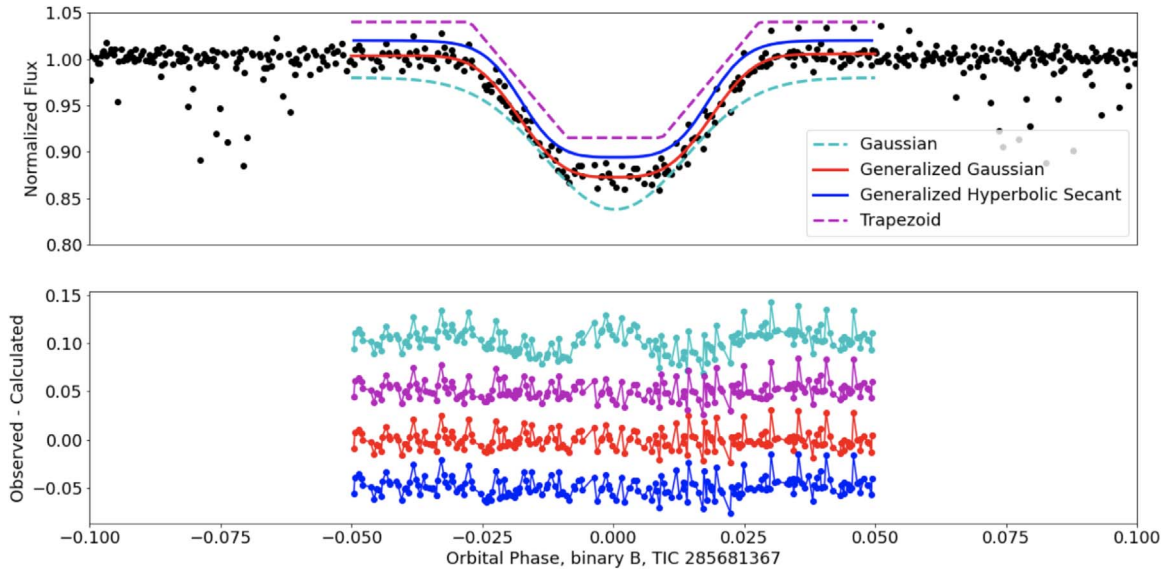
1. TIC 168789840: TIC 168789840 (TGV-96) is a confirmed (2+2) +2 hierarchical sextuple system consisting of an inner quadruple composed of two EBs and an outer EB (Powell et al. 2021). The two EBs of the quadruple have orbital periods of  $P_A = 1.31$  days and  $P_B = 1.57$  days and a mutual orbital period of about 4 yr. The third EB has an orbital period of



**Figure 10.** Upper panel: lightcurve for quadruple candidate TIC 392229331 exhibiting four sets of eclipses with two different periods. Second panel from top: trapezoid (magenta), Gaussian (cyan), generalized Gaussian (red), and generalized hyperbolic secant (blue) fits to the phase-folded, primary eclipses of binary A (zoomed in on phase between  $-0.1$  and  $0.1$ ). The blended eclipses have been removed, and the lightcurve has been detrended. The magenta, blue, and cyan curves are vertically offset for clarity. Third panel from top: residuals, in terms of (observed-calculated), for the four respective functions. Fourth panel from top: the undetrended, phase-folded lightcurve of binary A using the ephemeris determined by the fits to the individual eclipses. The secondary eclipse is clearly distinguished. The eclipses of binary B have been removed for clarity. Last panel: measured eclipse timing variations for the primary eclipses of binary A, showing no significant trends.

$P_C = 8.22$  days. The outer orbit of the sextuple has a period of about 2000 yr. The six stars have very similar masses ( $1.23\text{--}1.3 M_\odot$  for the primaries,  $0.56\text{--}0.66 M_\odot$  for the secondaries), sizes

( $1.46\text{--}1.69 R_\odot$  for the primaries,  $0.52\text{--}0.62 R_\odot$  for the secondaries), and effective temperatures ( $T_{\text{eff}} = 6350\text{--}6400$  K for the primaries,  $T_{\text{eff}} = 3923\text{--}4290$  K for the secondaries).



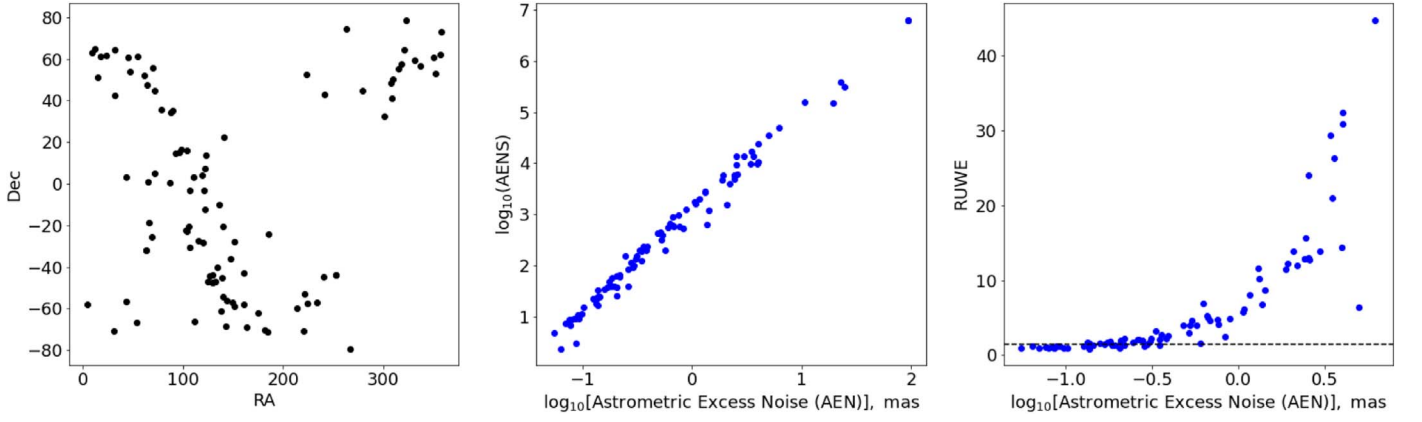
**Figure 11.** Same as the second and third panels in Figure 10 but for a primary eclipse of binary B of TIC 285681367 (see Figure 2). Here the generalized Gaussian and hyperbolic secant functions are clearly the better representation of the eclipse compared with a Gaussian. The flatter/sharper the eclipse bottom is, the better the former two fit the data.

**Table 1**  
Parameters of the Quadruple Candidates Presented Here

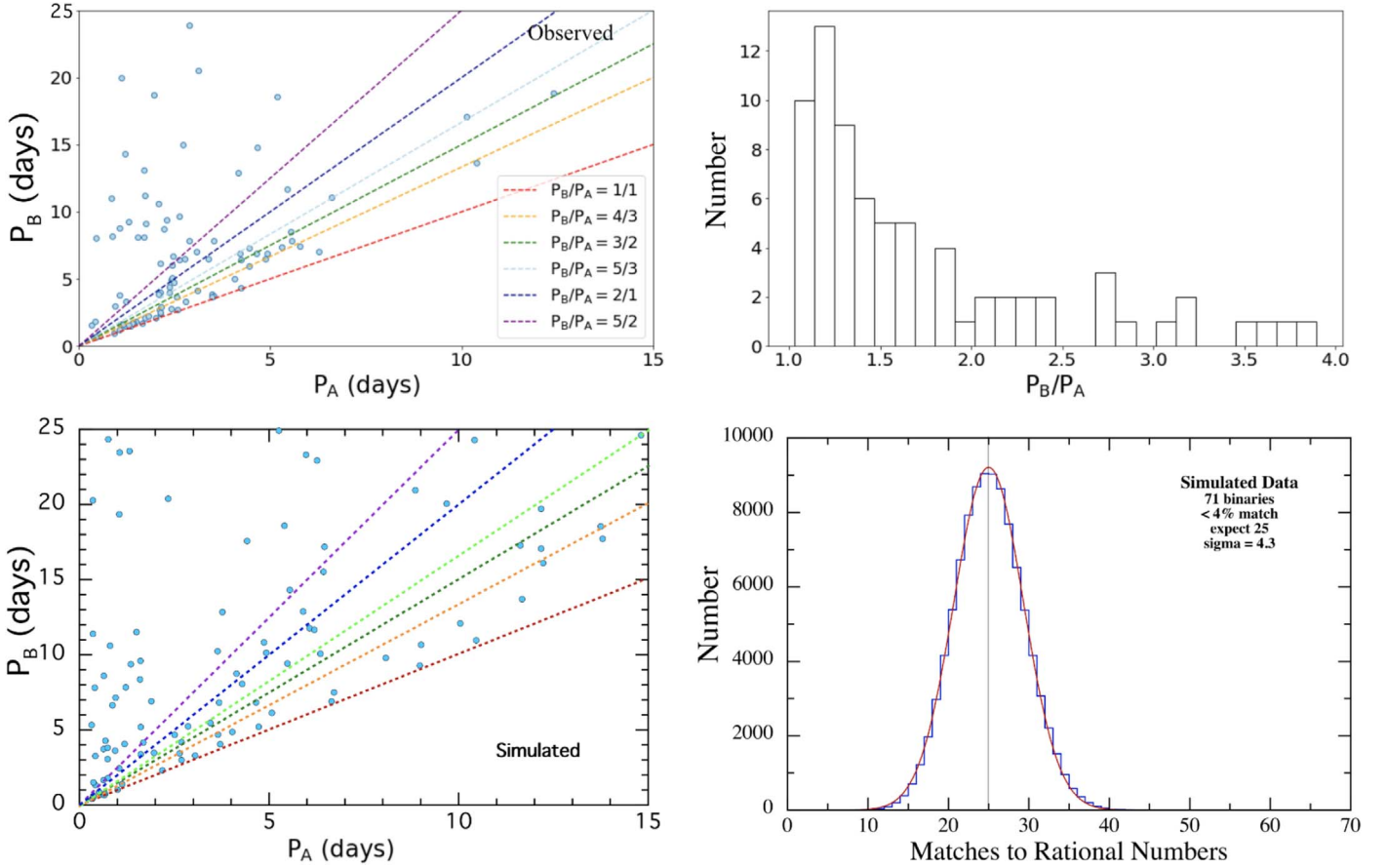
TIC ID	R.A. (deg)	Decl. (deg)	Binary	Period (days)	$T_0$ BJD−2,457,000	Phase <sub>s</sub>	Dep <sub>p</sub> (ppt)	Dep <sub>s</sub> (ppt)	Dur <sub>p</sub> (hr)	Dur <sub>s</sub> (hr)
9493888	69.510209	55.731524	A	2.098992	1816.2345	0.4999	146	117	2.9	2.7
			B	2.706156	1818.6919	0.5018	96	90	3.7	2.2
Additional information: TGV-1, Gaia EDR3 277142591660752128, $T_{\text{mag}}$ : 11.98, $T_{\text{eff}}$ : 5112 K, Dist: 374.29 pc										
Comments A: ...										
Comments B: ...										
25818450	352.743444	53.069150	A	10.132402	1769.9109	0.6396	12	9	...	...
			B	17.101657	1765.8009	...	80	...	...	...
Additional information: TGV-2, Gaia EDR3 1992486494566143744, $T_{\text{mag}}$ : 11.14, $T_{\text{eff}}$ : 7172 K, Dist: 838.61 pc										
Comments A: depth difference between sectors.										
Comments B: depth difference between sectors.										
27543409	122.702004	13.567217	A	2.122862	1493.1001	0.4964	50	15	...	...
			B	4.013356	1494.513	...	75	...	...	...
Additional information: TGV-3, Gaia EDR3 653620084592824960, $T_{\text{mag}}$ : 13.22, $T_{\text{eff}}$ : 6421 K, Dist: 1878.88 pc										
Comments A: ...										
Comments B: S/N too low for secondary measurements.										
31928452	53.969191	−66.936899	A	2.8823	1337.9129	0.5014	30	25	2.1	1.6
			B	7.829944	1326.0719	0.5584	89	72	3.2	3.4
Additional information: TGV-4, Gaia EDR3 4670910529358997888, $T_{\text{mag}}$ : 13.28, $T_{\text{eff}}$ : ..., Dist: 574.18 pc										
Comments A: Ellipsoidal variations; potential depth differences between sectors.										
Comments B: Potential depth differences between sectors.										
45160946	147.614561	−36.191917	A	3.516299	1544.8002	0.4989	35	20	2.9	2.2
			B	7.846200	1550.438	0.4954	125	75	5.9	6.8
Additional information: TGV-5, Gaia EDR3 5434831348413276160, $T_{\text{mag}}$ : 13.21, $T_{\text{eff}}$ :—K, Dist: 446.90 pc										
Comments A: Prominent ETVs; compact 2+2 quadruple system; contaminator for TIC 45160944; nearly blended with TIC 872919203.										
Comments A: Prominent ETVs; compact 2+2 quadruple system; contaminator for TIC 45160944; nearly blended with TIC 872919203.										

**Note.** TGV-N = TESS/Goddard/VSG quadruple candidate-N; Phase<sub>s</sub> = secondary phase, Dep<sub>n</sub> = depth of eclipse n, Dur<sub>n</sub> = duration of eclipse n, Teff = composite effective temperature, ppt = parts per thousand.

(This table is available in its entirety in machine-readable form.)



**Figure 12.** Left panel: R.A. and decl. of the quadruple candidates in this catalog. Middle panel: the respective astrometric\_excess\_noise (AEN) and astrometric\_excess\_noise\_sig (AENS) as measured by Gaia. We note that both are on a logarithmic scale. Right panel: corresponding distribution of the renormalized unit weight error (RUWE) as a function of the AEN. The dashed horizontal line indicates  $\text{RUWE} = 1.5$ , the value above which the astrometry is likely affected by a presumptive wide companion.



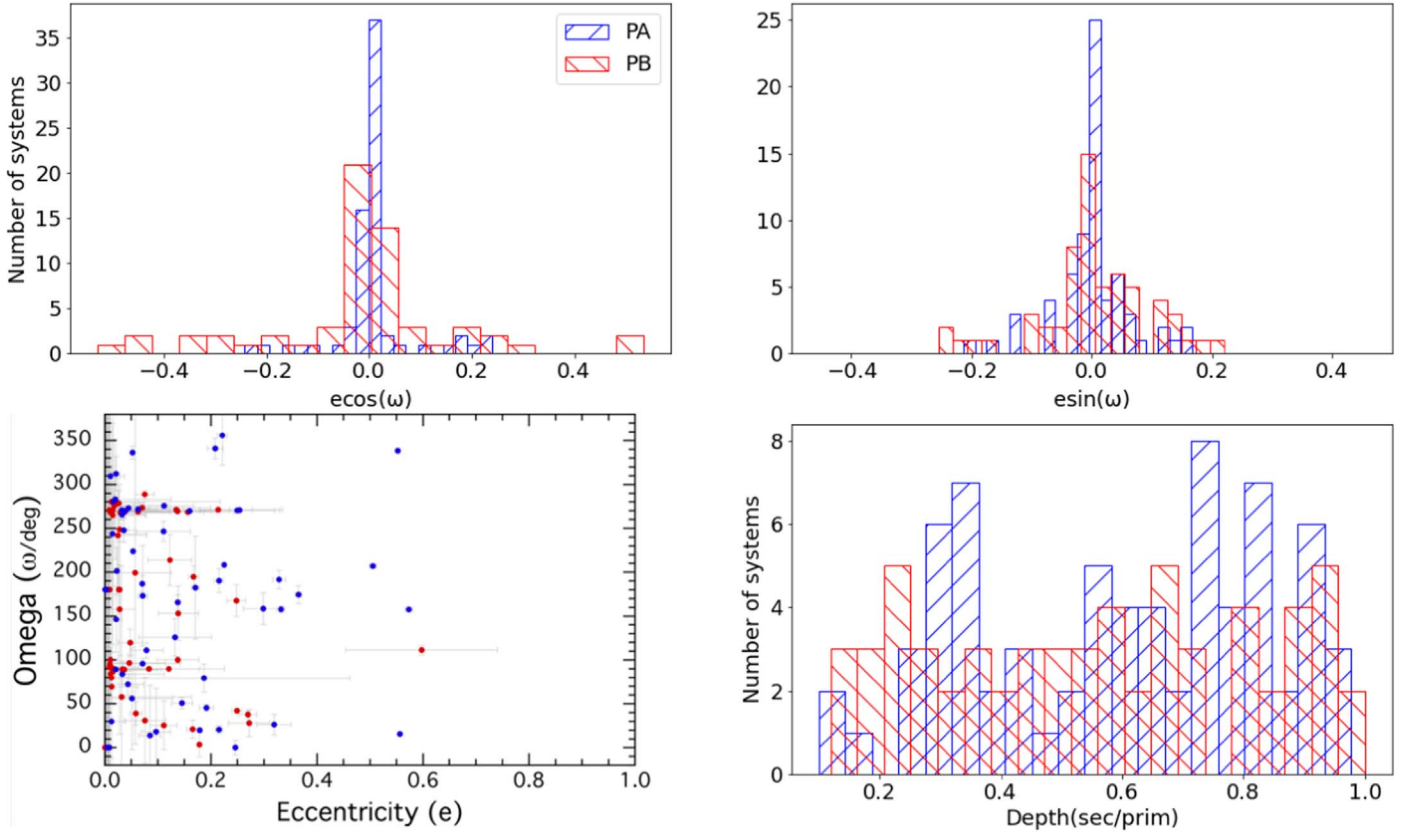
**Figure 13.** Upper left: measured period ratios between  $P_B$  and  $P_A$  for the 97 quadruple candidates from TESS that pass vetting tests, compared with select integer ratios. Upper right: distribution of the number of systems with periods ratio  $P_A/P_B$  smaller than 4 (72 out of 97 systems). Lower left: same as upper left but for a simulated set of systems. Lower right: number of simulated systems with period ratios that match to within 4% one of the rational numbers 1:1, 5:4, 4:3, 3:2, 5:3, 2:1, 5:2, or 3:1. See text and Table 3 for details.

2. TIC 454140642: TIC 454140642 (TGV-89) is a confirmed 2+2 hierarchical quadruple system composed of two EBs that exhibit strong dynamical interactions and eclipse timing variations (Kostov et al. 2021b). The two EBs have orbital periods of  $P_A = 10.3928$  days and  $P_B = 13.6239$  days and a mutual orbital period of about 432 days. The entire system is practically coplanar, with mutual inclinations

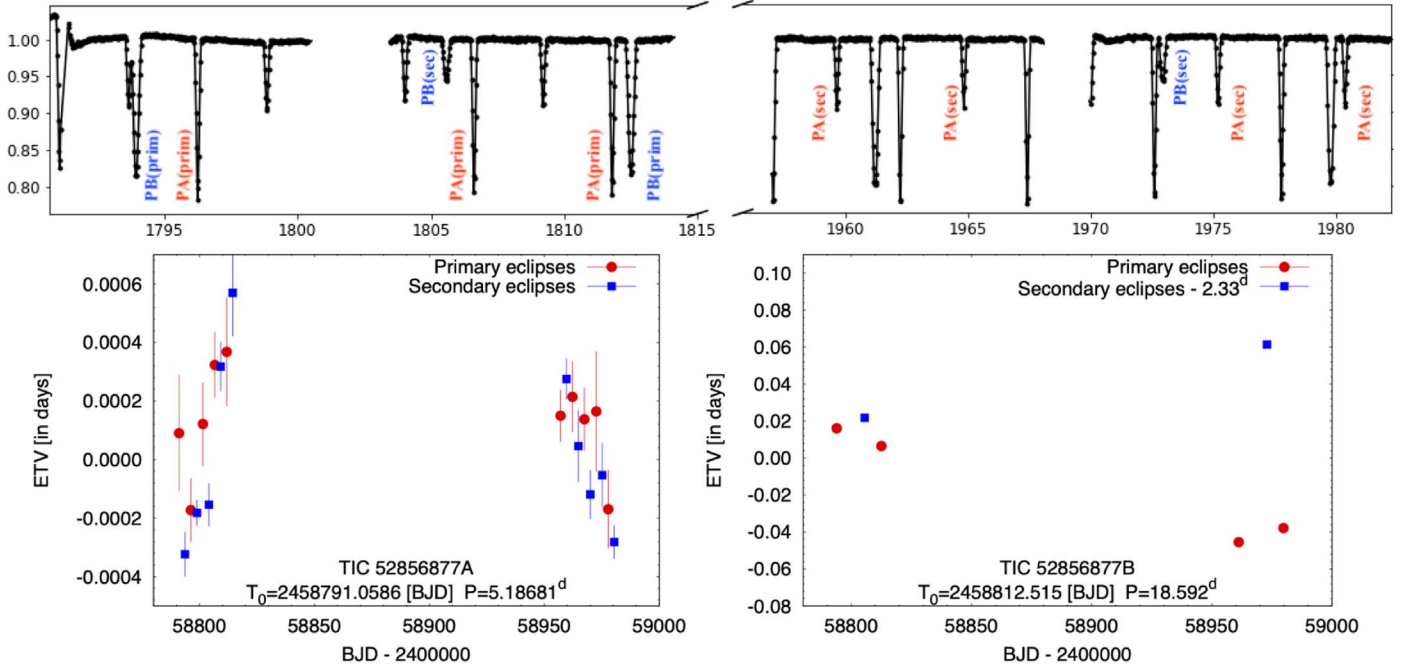
smaller than  $0.5^\circ$ . The four stars have very similar masses ( $1.11\text{--}1.2 M_\odot$ ), sizes ( $1.1\text{--}1.26 R_\odot$ ), and effective temperatures ( $T_{\text{eff}} = 6188\text{--}6434$  K).

3. TIC 52856877: TIC 52856877 (TGV-6) is a candidate 2+2 hierarchical quadruple system composed of two EBs with orbital periods of  $P_A = 5.1868$  days and  $P_B = 18.5864$  days. For simplicity, throughout this manuscript we label

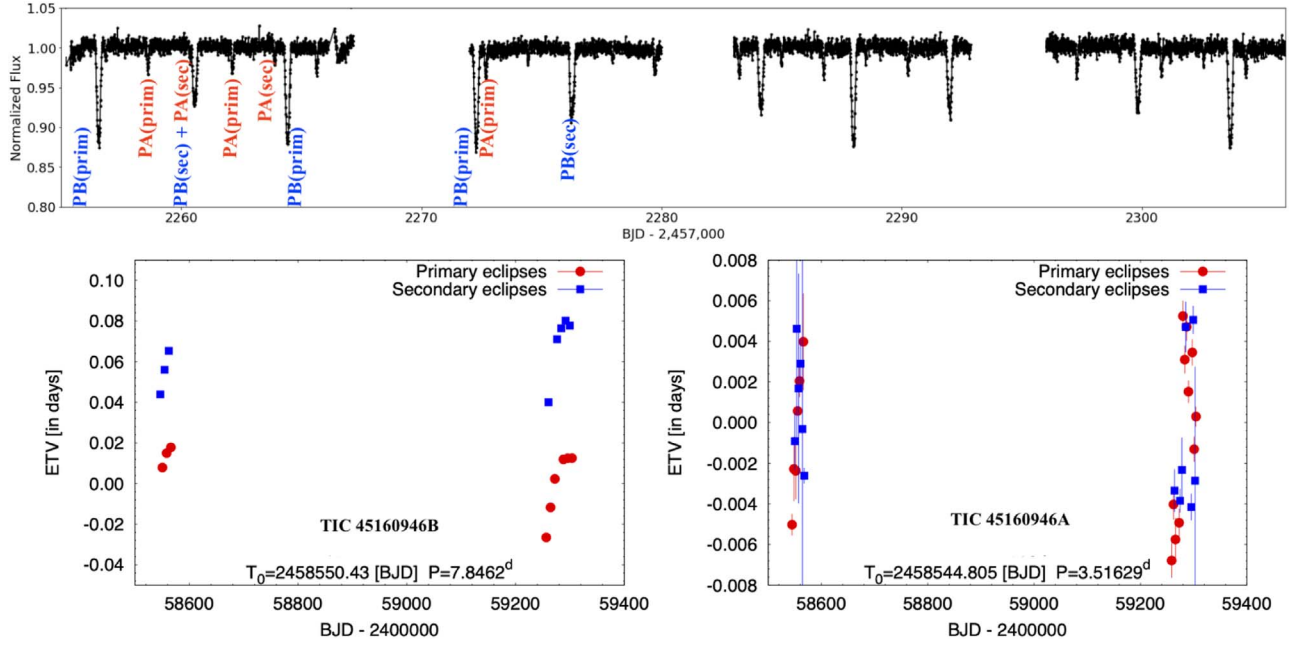




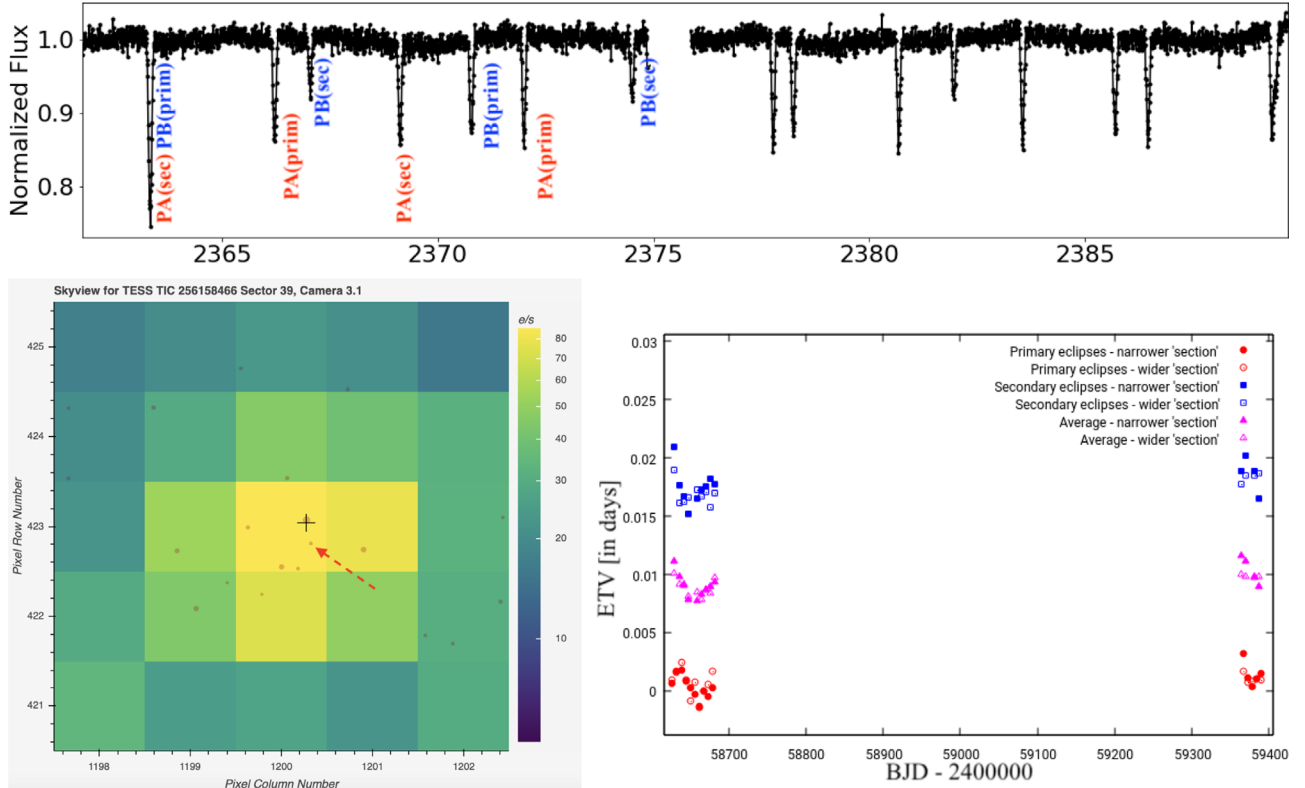
**Figure 14.** Upper panels: measured  $e \cos(\omega)$  (left panel) and  $e \sin(\omega)$  (right panel) for the corresponding binary A (blue) and B (red) for each quadruple candidate exhibiting both primary and secondary eclipses. Most  $e \cos(\omega)$  and  $e \sin(\omega)$  ratios cluster around zero. Lower left panel: corresponding eccentricity and omega values with the associated measured uncertainties, calculated by propagating the uncertainties in  $e \cos(\omega)$  and  $e \sin(\omega)$  into those for  $e$  and  $\omega$ . Lower right panel: eclipse depth ratios, showing no clear preference.



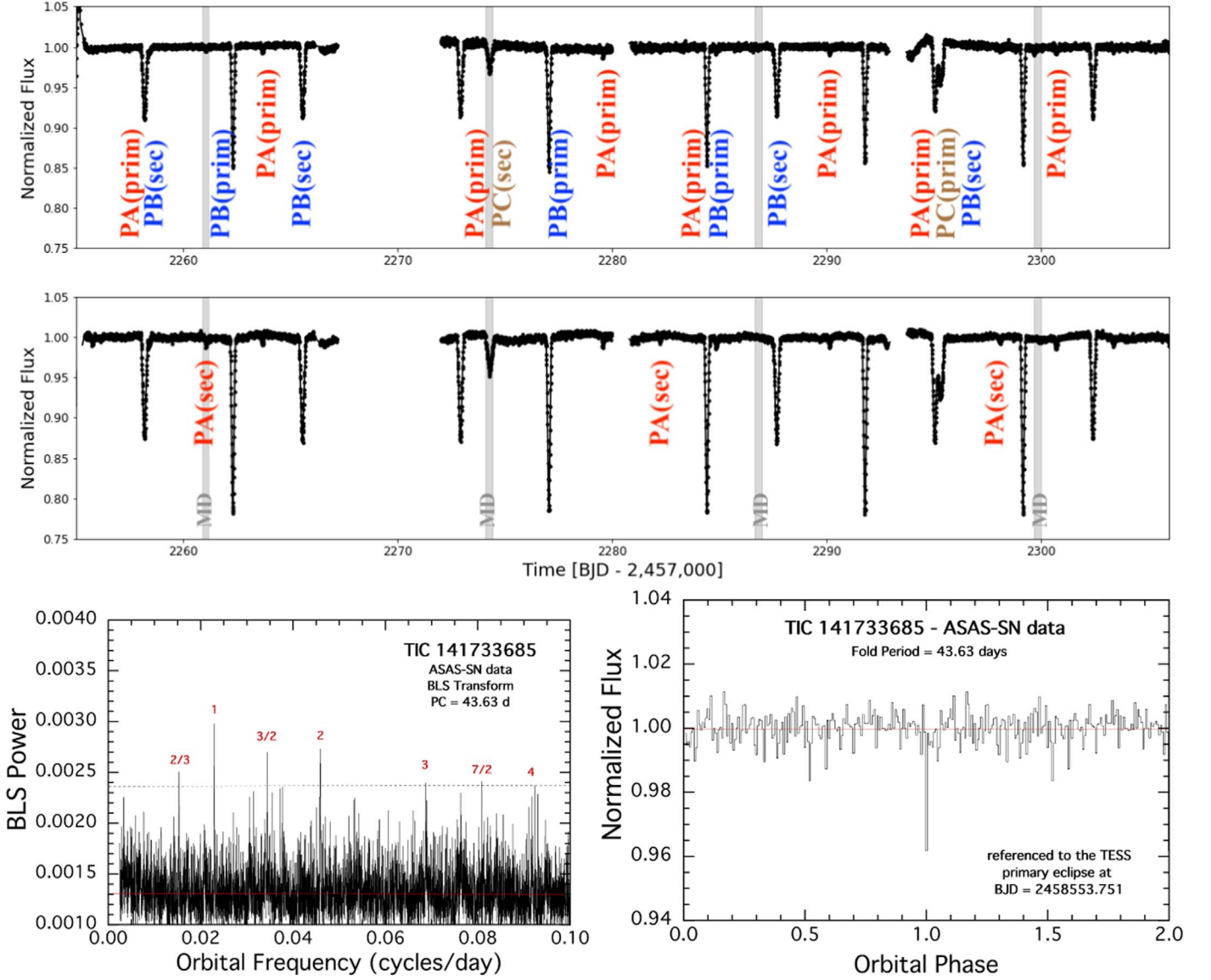
**Figure 15.** Upper panel: FFI lightcurve of quadruple candidate TIC 52856877. The system consists of two EBs with  $P_A = 5.1868$  and  $P_B = 18.5864$  days, highlighted in the figure. Lower panels: measured eclipse-time variations for  $P_A$  (left panel) and  $P_B$  (right panel), indicating dynamical interactions between the two binaries and suggesting that the system is gravitationally bound.



**Figure 16.** Same as Figure 15 but for quadruple candidate TIC 45160946. The system consists of two EBs with  $P_A = 3.5163$  and  $P_B = 7.8462$  days, highlighted in the figure. Lower panels: measured eclipse-time variations for  $P_A$  (left panel) and  $P_B$  (right panel), indicating dynamical interactions between the two binaries and suggesting that the system is gravitationally bound.



**Figure 17.** Upper panel: same as Figure 15 but for quadruple candidate TIC 256158466. The system consists of two EBs with  $P_A = 5.7745$  and  $P_B = 7.4544$  days, highlighted in the figure, both on target. Lower left panel: Skyview image of the target for sector 39, showing all Gaia sources down to  $G = 21$  mag. We note that compared with Skyview images shown above, here the image is zoomed in to a size of  $5 \times 5$  pixels in order to highlight the position of the nearby field star TIC 1508756606 ( $5''/65$  separation,  $\Delta T \approx 4.8$  mag fainter, marked with dashed red arrow). TIC 1508756606 has parallax and proper motion within  $1\sigma$  of those of the target star and thus might be in a comoving quintuple system with the quadruple TIC 256158466. Third panel: measured eclipse-time variations for  $P_A$  using two lightcurve sections centered on each eclipse—narrow and wide—show potential sine-like variations only in the former case.



**Figure 18.** First panel from top: same as Figure 17 but for quadruple candidate TIC 141733685, showing the sectors 35 and 36 *eleanor* data. The target exhibits three EBs with  $P_A = 5.29$  days,  $P_B = 7.37$  days, and  $P_C = 43.63$  days, as highlighted in the figure. Second panel: same as first panel but showing the FITSH lightcurve. Lower left panel: BLS transform of the ASAS-SN archival data for TIC 141733685 after removing binary A from the data train. The transform is plotted as a function of frequency in order to better identify harmonics. The orbital period of binary C is found to be 43.63 days ( $\nu = 0.02292$  cycles/day). This peak is marked as “1” for the first harmonic. Other harmonics and subharmonics are also marked in red. Nearly all of the highest peaks (i.e., above the dotted line) are due to this period or its associated harmonics. Lower right panel: folded, binned, and averaged lightcurve from the ASAS-SN archival data. There are 150 phase bins in the plot, each corresponding to  $\sim 0.3$  days. The phasing is referenced to one of the TESS-detected primary eclipses. There is also a likely secondary eclipse near phase 0.5, but its statistical significance is much less than that of the primary eclipse.

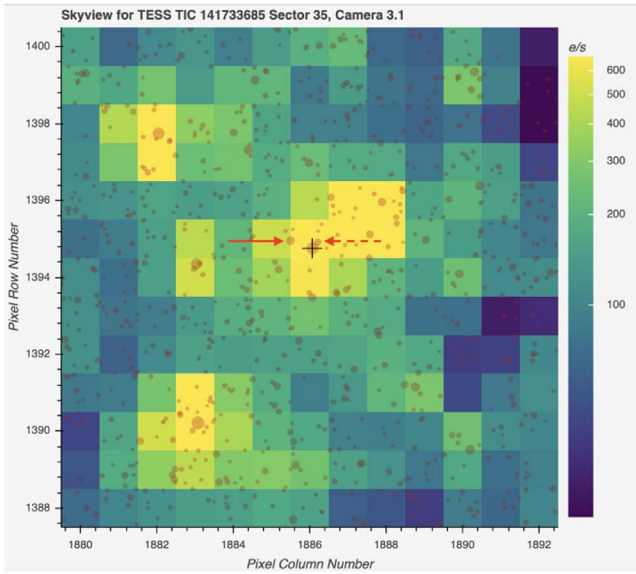
the periods of the two EBs as sorted in ascending order. The target was observed in sectors 18 and 24; the TESS lightcurve of the system is shown in Figure 15. The system exhibits strong eclipse timing variations, as seen from Figure 15. Gaia EDR3 shows AEN = 0.31 mas with an AESN of 150.57 and RUWE = 2.19. Altogether, these considerations indicate kinematic motions between the two EBs and suggest that the system is gravitationally bound. The analysis of the system, including follow-up observations, is in progress.

4. TIC 45160946: TIC 45160946 (TGV-5) is a candidate 2+2 hierarchical quadruple system composed of two EBs with orbital periods of  $P_A = 3.5163$  days and  $P_B = 7.8462$  days. The target was observed in sectors 9, 35, and 36; the

TESS lightcurve for the latter two is shown in Figure 16. As in the case for TIC 52856877, TIC 45160946 also exhibits strong eclipse timing variations (see Figure 16). Gaia EDR3 shows AEN = 3.6 mas, with an AESN of 13472, and RUWE = 26.33. This indicates kinematic motions between the two EBs and suggests that the system is gravitationally bound with a relatively short outer orbital period. A detailed analysis of the system is in progress.

5. TIC 256158466: TIC 256158466 (TGV-37) is a candidate 2+2 hierarchical quadruple system composed of two EBs with orbital periods of  $P_A = 5.7745$  days and  $P_B = 7.4544$  days, with nearly identical primary and secondary eclipses for  $P_A$  (depths of 131 parts per thousand [ppt] and 128 ppt,





**Figure 19.** Skyview image of TIC 141733685 (black plus symbol) for sector 35, showing all Gaia sources brighter than  $G = 21$  mag. There is a nearby field star, TIC 141733688 (dashed arrow), separated from the target by  $4''.53$ , and with magnitude difference  $\Delta T \approx 3.15$  mag. Another field star, TIC 141733701 (solid arrow), has a separation of  $12''.6$  and magnitude difference  $\Delta T \approx 2.03$  mag. TIC 141733685 and TIC 141733688 have comparable parallax and, to a lesser degree, proper motion. See text for details.

respectively). The target was observed in sectors 12, 13, and 39; the TESS lightcurve for the latter is shown in Figure 17. Our analysis shows potential sinusoidal variations for the times of the  $P_A$  eclipses, although the variations only appear if we use relatively narrow sections of the lightcurve centered on the corresponding eclipses. If we use somewhat wider sections of the eclipses, the variations disappear in the scatter, as demonstrated in Figure 17. Thus we label this target as showing potential ETVs.

We also note that there is a nearby field star, TIC 1508756606, with a separation of  $5''.65$ , coordinates of R.A. =  $17:47:35.21$  and decl. =  $-79:22:40.94$ , and magnitude difference  $\Delta T \approx 4.8$  mag. Our analysis rules out TIC 1508756606 as a source of either  $P_A$  or  $P_B$ . The coordinates of TIC 1508756606, along with Gaia’s parallax ( $1.26 \pm 0''.32$  vs.  $1.4 \pm 0''.02$  for TIC 256158466) and proper motion (pmRA =  $0.54 \pm 0.3$  mas yr $^{-1}$ , pmDec =  $-29.57 \pm 0.36$  mas yr $^{-1}$  vs. pmRA =  $-0.92 \pm 0.02$  mas yr $^{-1}$ , pmDec =  $-29.18 \pm 0.02$  mas yr $^{-1}$  for TIC 256158466), suggest that it might in fact form a comoving quintuple system with TIC 256158466. Gaia’s EDR3 AEN for both targets is zero, and the corresponding RUWE is about 0.96.

6. TIC 141733685: The lightcurve of TIC 141733685 (TGV-95) exhibits three EBs. The target was observed in sectors 8, 9, 35, and 36. Two of the EBs have orbital periods of  $P_A = 5.29$  days and  $P_B = 7.37$  days. We note that the former is seen in *eleanor* data only in sectors 35 and 36, where it is unclear whether the period is 5.29 days or half of that. To account for this, we extract the target’s lightcurve using the *FITSH* pipeline (Pál 2012), which shows the primary and secondary eclipses of  $P_A$  in all four sectors of data. The third EB shows three eclipses, but it is unclear from TESS data whether its period,  $P_C$ , is  $\sim 21.8$  days or  $\sim 43.6$  days. This is because one of three eclipses

coincides with a momentum dump in sector 35 and is blended with a  $P_A$  eclipse, and another (in sector 36) is blended with a  $P_A$  primary and a  $P_B$  secondary. The *eleanor* and *FITSH* lightcurves for sectors 35 and 36 are shown in Figure 18. Analysis of archival All-Sky Automated Survey for Supernovae (ASAS-SN) data for TIC 141733685 shows a clear periodicity at  $P_C = 43.63$  days with primary and secondary eclipses and a slight eccentricity. We note that TIC 141733685 contaminates the TESS *eleanor* lightcurve of TIC 141733683 and TIC 141733701.

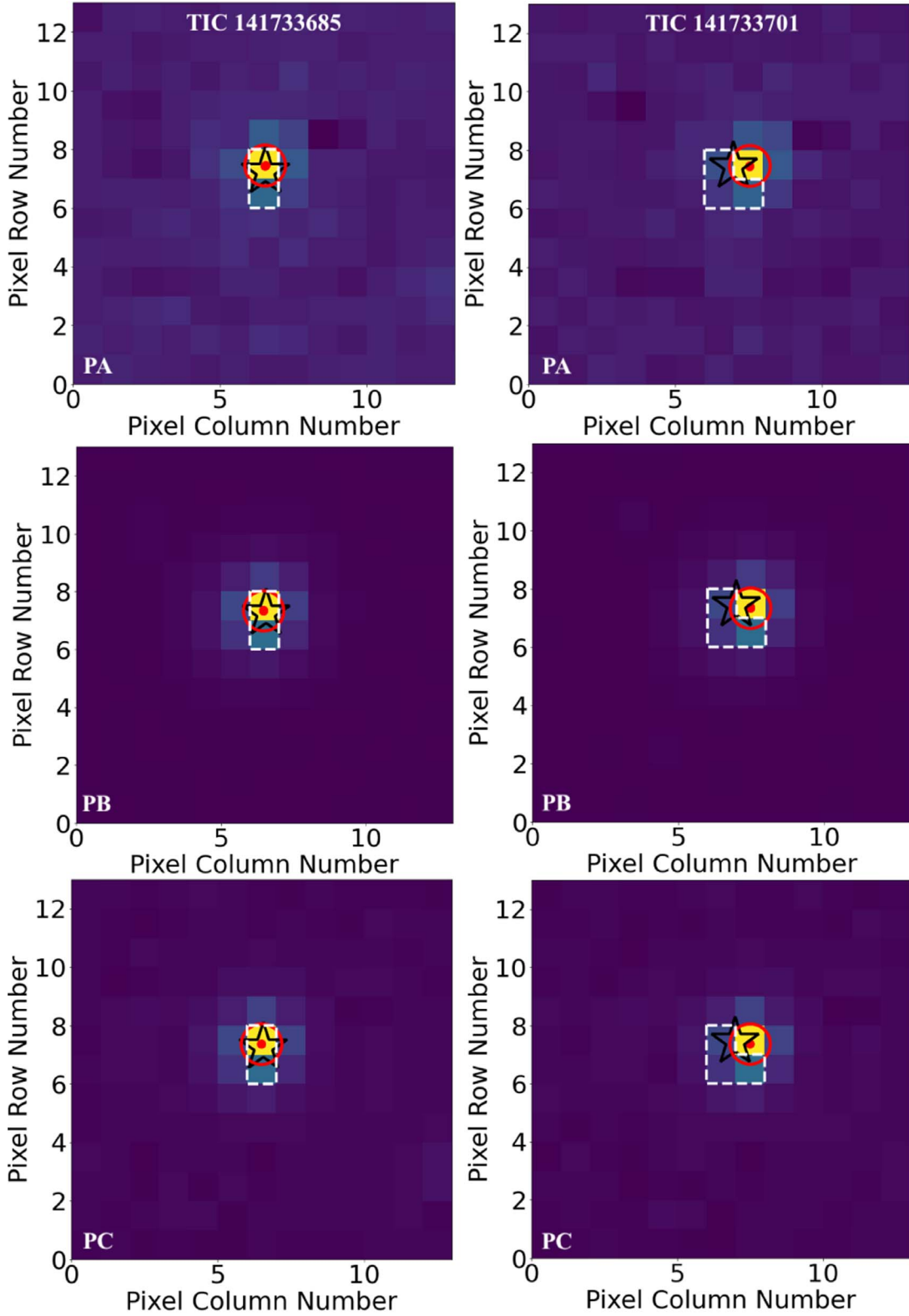
Closer inspection of the field around TIC 141733685 shows that there is a nearby field star, TIC 141733688, with a separation of  $4''.53$ , coordinates of R.A. =  $08:39:24.8$  and decl. =  $-47:21:39.85$ , and magnitude difference  $\Delta T \approx 3.15$  mag (see Figure 19). This field star is not bright enough to produce the  $P_B$  or  $P_C$  eclipses as the needed  $\Delta T < 0.9$  mag and  $\Delta T < 2.06$  mag, respectively. TIC 141733688 is bright enough to produce the  $P_A$  eclipses (needed  $\Delta T < 4.05$  mag). Another field star, TIC 141733701, has a separation of  $12''.6$  and magnitude difference of ( $\Delta T \approx 2.03$  mag) and is nominally bright enough to produce all three sets of eclipses.

As seen from Figure 20, our photocenter analysis clearly rules out the nearby TIC 141733701 as a potential source of the detected eclipses and shows that all three EBs originate from the position of TIC 141733685. However, the measurement is not precise enough to distinguish between TIC 141733685 and TIC 141733688 for  $P_A$  as the eclipses are very shallow and the separation very small. Thus the source of  $P_A$  can be either TIC 141733685 or TIC 141733688. With that said, the  $P_A$  photocenters for TIC 141733685 “pull” away from TIC 141733688 (first row of panels, Figure 20), indicating that the latter is not a likely source. Overall, these considerations suggest that there are two possibilities for the structure of the system: (1) quadruple ( $P_B + P_C$ ) on TIC 141733685,  $P_A$  on TIC 141733688; or (2) sextuple ( $P_A + P_B + P_C$ ) on TIC 141733685. Furthermore, the measured ETVs for both  $P_A$  and  $P_B$  imply nonlinear effects (more prominent for  $P_B$ , see Figure 21), which strengthens the sextuple interpretation.

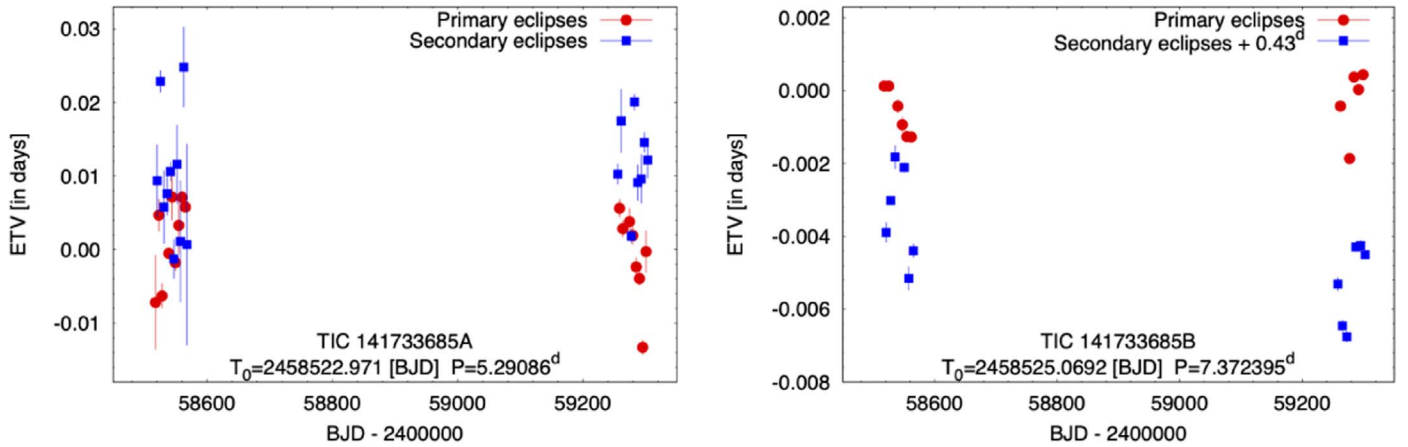
Gaia EDR3 measurements show AEN = 0.085 mas, with an AENS of 9.19, and RUWE = 0.95 for TIC 141733685. The target’s parallax is within  $1\sigma$  of that for TIC 141733688,  $0.55 \pm 0.01$  mas for the former versus  $0.58 \pm 0.03$  mas for the latter. The corresponding proper motions are comparable, 7.25 mas versus 7.45 mas, respectively, although the proper motions in decl. are nominally different at a greater than  $3\sigma$  level: (pmRA =  $-6.12 \pm 0.03$  mas yr $^{-1}$ , pmDec =  $3.89 \pm 0.04$  mas yr $^{-1}$ ) versus (pmRA =  $-6.08 \pm 0.02$  mas yr $^{-1}$ , pmDec =  $4.3 \pm 0.02$  mas yr $^{-1}$ ). Thus TIC 141733685 and TIC 141733688 might be a comoving system, in which case possibility (2) above would represent a septuple at a projected separation of  $\sim 8000$  au. Given the magnitude and early spectral type of both sources, the prospect of spectroscopic follow-up might be poor.

Finally, we note that the coordinates of TIC 141733685 (R.A. =  $08:39:25.2$ , decl. =  $-47:21:38.36$ ) also coincide with those of the open Galactic cluster [KPS2012] MWSC 1523 (R.A. =  $08:39:27$ , decl. =  $-47:21.4$ , Monteiro et al. 2020, MNRAS, 499, 1874). The proper motion of two are, however, different: (pmRA =  $-6.08 \pm 0.01$  mas yr $^{-1}$ ,





**Figure 20.** Photocenter analysis for  $P_A = 5.29$  days (first row from top),  $P_B = 7.37$  days (second row), and  $P_C = 43.63$  days (third row) for TIC 141733685 (left panels) and the nearby field star TIC 141733701 (right panels) using sector 35 data. The panels show the corresponding difference images along with the location of the respective target on the detector (black star, label “TIC”), the measured per-eclipse photometers (small red symbols, label “Indiv Cent”), and the average photometers (large red symbols, label “Avg Cent”). The dashed white contours indicate the aperture used by *eleanor* for the respective target. For  $P_C$ , there is a single eclipse detected in this sector (see Figure 18), corresponding to a single photometer measurement. Our analysis clearly rules out TIC 141733701 as a potential source of  $P_A$ ,  $P_B$ , and  $P_C$  (right panels) and confirms that all three EBs are associated with TIC 141733685 (left panels). We note that the sky orientation of Figure 19 is flipped along the  $x$ -axis (i.e.,  $x \rightarrow -x$ ) with respect to the images shown here.



**Figure 21.** Measured ETVs for  $P_A$  (left) and  $P_B$  (right) for TIC 141733685, showing nonlinear effects and indicating that the two are likely to be gravitationally bound.

$\text{pmDec} = 4.29 \pm 0.01 \text{ mas yr}^{-1}$ ) for TIC 141733685 versus (average  $\text{pmRA} = -4.12 \pm 0.77 \text{ mas yr}^{-1}$ ,  $\text{pmDec} = 8.37 \pm 0.77 \text{ mas yr}^{-1}$ ) for MWSC 1523.

7. TIC 1337279468: The lightcurve of TIC 1337279468 (TGV-97) exhibits three EBs with orbital periods  $P_A = 4.45$  days,  $P_B = 5.94$  days, and  $P_C = 10.57$  days. The target was observed in sectors 12 and 39. The TESS lightcurve for the latter is shown in Figure 22. We note that the TIC lists a source at a separation of  $0''.59$  (TIC 246039685) and another at a separation of  $4''.84$  (TIC 246039695). Neither is present in the Gaia EDR3 data.

There are three nearby field stars (TIC 1337279457, TIC 1337279471, and TIC 1337279458) with separations of  $\sim 4''$ – $6''$  and magnitude differences  $\Delta T \sim 5.5$ – $6$  mag (see Figure 23). None of these is bright enough to produce the eclipses seen in the lightcurve as the shallowest primary eclipses ( $P_B$ , depth  $\sim 25$  ppt) require a magnitude difference of  $\Delta T < 3.2$  mag. Our photocenter analysis indicates that all three sets of eclipses are on target (Figure 22), and, accordingly, we consider the system to be a likely sextuple. At the time of writing, there are insufficient data to evaluate its hierarchy and structure.

Gaia EDR3 shows  $\text{AEN} = 2.43$  mas, with an AENS of 5891, and  $\text{RUWE} = 12.82$  for TIC 1337279468. The target's proper motion is within  $\sim 1\sigma$  of those for TIC 1337279471, and the two might be a potential comoving septuple. However, the proper motions are small and the parallax accuracy is relatively low (the EDR3 parallax for TIC 1337279471 is  $0.4 \pm 0.5$  mas), so it is currently unclear whether this is the case.

Finally, we note that there is another EB in the  $13 \times 13$  TESS pixels surrounding TIC 1337279468—TIC 246039698—separated by about 4 pixels. The ephemeris of TIC 246039698 is unrelated to any of the three EBs of TIC 1337279468.

8. TIC 438226195: TIC 438226195 (TGV-85) produced a single extra transit-like event in sector 6 near time  $t = 1488.8598$  (see Figure 24). Our analysis indicates that the feature is on target, and, as we suspected this to be a candidate for a circumbinary planet, we added the target for 2 minutes' cadence observations with TESS through the DDT program (number 27). It was observed again in sector 33 and indeed produced another clear extra transit-like event, strengthening the circumbinary planet hypothesis. However, closer inspection of the sector 33 lightcurve

showed that the first secondary eclipse of the main EB, about 11.7 days before the clear extra event, is deeper than the rest—the trademark signature of a blend between two events. This indicated that the extra events are due to a second, on-target, EB, making this a quadruple candidate.

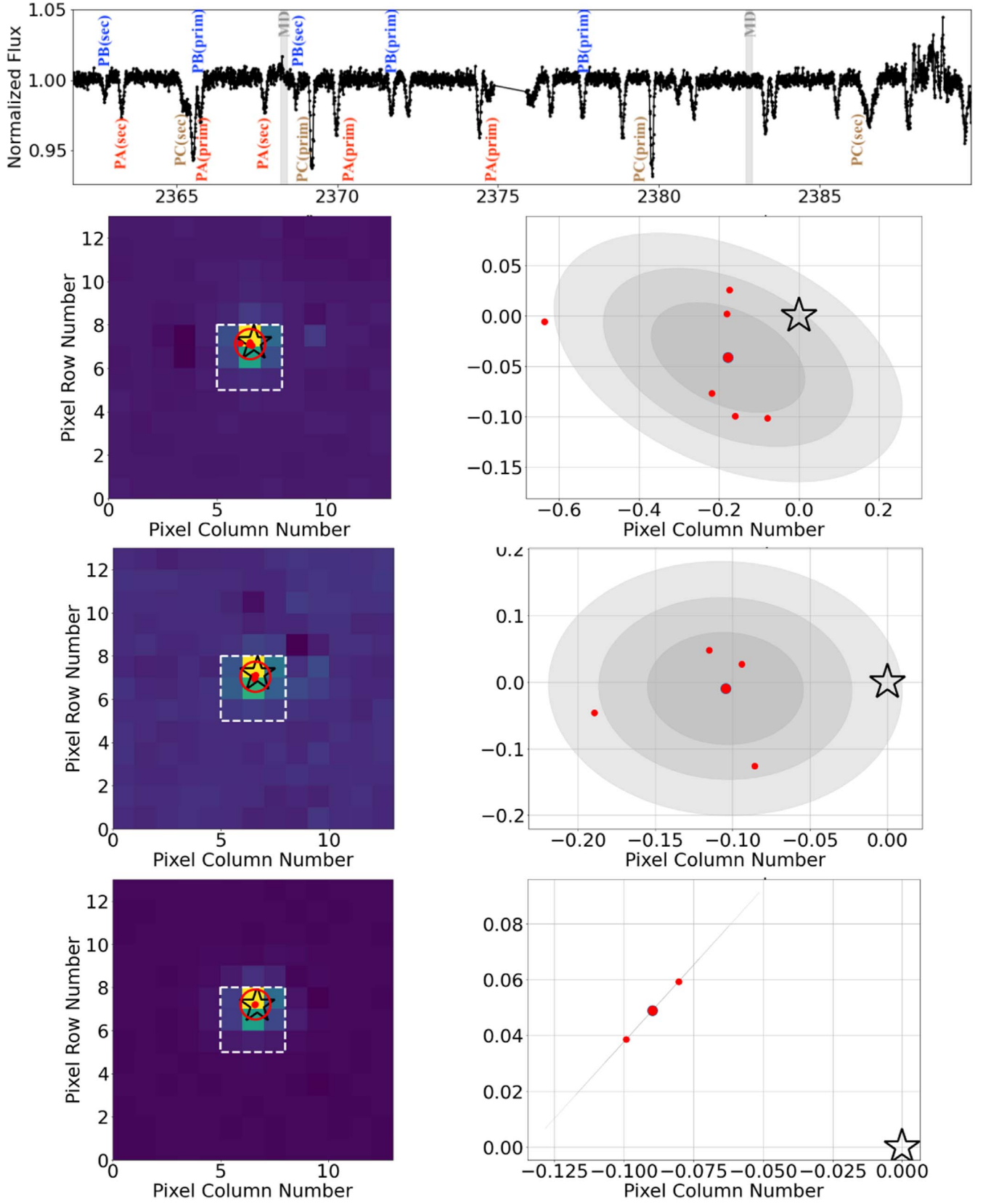
#### 5.4.2. Crossmatch with Archival Data

The results presented here can be further used to compare the measured ephemerides from TESS, especially for targets with multisector observations, to available archival photometric data from, for example, ASAS-SN (Shappee et al. 2014; Kochanek et al. 2017), Digital Access to a Sky Century @ Harvard (DASCH, Grindlay et al. 2012), Hungarian-made Automated Telescope Network (HATNet, Bakos et al. 2004), Kilodegree Extremely Little Telescope (KELT, Pepper et al. 2007), Kepler/K2 (Borucki et al. 2010), Northern Sky Variability Survey (NSVS, Woźniak et al. 2004), Optical Gravitational Lensing Experiment (OGLE, Udalski et al. 1992), and Wide Angle Search for Planets (WASP, Pollacco et al. 2006). Such a comparison could also allow testing for potential apsidal motion, which, if large enough to be readily detected, would strengthen the case for a genuine quadruple system.

As an example of this approach, we show on Figure 25 the DASCH data of TIC 172900988. This is an EB system hosting a transiting circumbinary planet (Kostov et al. 2021a) and exhibiting clear apsidal motion. While the cadence of the DASCH observations is low and there are very few in-eclipse data points, the phase change of the secondary eclipse relative to the primary is clearly seen in the phase-folded DASCH data, and the two eclipses follow slightly different periods. However, checking the archival data for the bulk of our 97 targets is beyond the scope of this paper.

Another potential comparison can be with spectroscopic archives. For example, Kounkel et al. (2021) examined the APOGEE DR16 and DR17 for double-lined spectroscopic binaries. They detected several SB2 with corresponding eclipses in TESS data—demonstrating the crossmatch potential—and uncovered 813 SB3 and 19 SB4 systems. One of the targets in our catalog, TIC 219469945, is listed as an SB3 system in the Kounkel et al. (2021) database. None is listed as SB4.

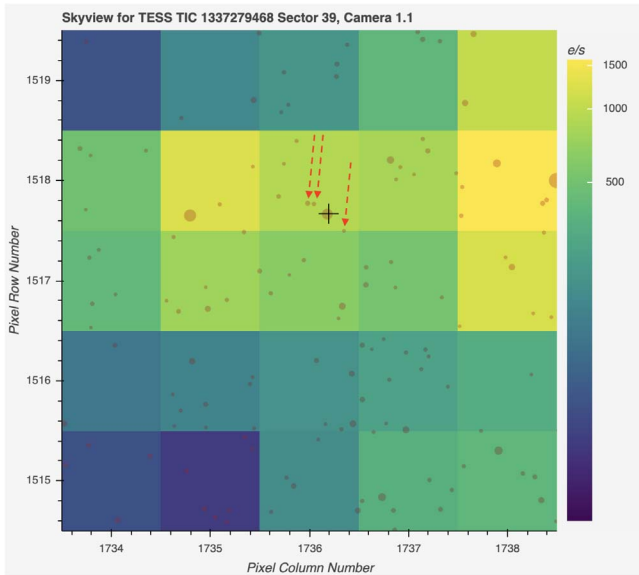
Finally, the targets in our catalog can be compared to astrometric binary stars detected by Gaia, especially those with



**Figure 22.** Upper panel: *eleanor* lightcurve for sextuple candidate TIC 1337279468, showing the sector 39 data. The target exhibits three EBs with  $P_A = 4.45$  days,  $P_B = 5.94$  days, and  $P_C = 10.57$  days, as highlighted in the panel. Second, third, and fourth rows: photocenter analysis of TIC 1337279468 for  $P_A$  (second row),  $P_B$  (third row), and  $P_C$  (fourth row) for sector 39. The right panels show zoom-ins on the central pixel along with the corresponding confidence intervals (gray colors,  $1\sigma$ ,  $2\sigma$ , and  $3\sigma$ , respectively) of the scatter in the measured photocenters. We note that there are only two eclipses of binary  $P_C$  in this sector, corresponding to two measured photocenters, and thus the measured offset of 0.1 pixels (fourth row, right panel) is not significant. Thus all three EBs originate from TIC 1337279468.

**Table 2**Ephemerides Crossmatch between the Quadruple Candidates Presented Here and  $\sim 30,000$  Unvetted EB Candidates from the GSFC TESS EB Catalog (E. Kruse et al. 2022, in preparation)

TIC	Period	$T_0$	R.A.	Decl.	Sectors Obs.	Comments
63459761	4.3621	1683.8108	308.5251	41.1359	14-15	contamination
63459765	4.3621	1683.8113	308.5181	41.1355	14-15, 41	
63459804	4.3621	1683.8125	308.5183	41.1309	14-15, 41	
63459811	4.3620	1683.8125	308.5300	41.1297	14-15, 41	
283940788	0.8768	1765.3137	8.8514	62.9015	17-18, 24	coincidence
285609529	0.8767	1683.7647	296.2538	26.1412	14, 40-41	
285609535	0.8767	1683.7647	296.2518	26.14063	14, 40-41	
370440624	2.2350	1572.7416	143.2320	-68.6811	9-11, 36-38	coincidence
451982722	2.2334	1684.4948	296.5768	27.0600	14, 41	
451982756	2.2334	1684.4950	296.5829	27.0637	14, 41	



**Figure 23.**  $5 \times 5$  pixels Skyview image of TIC 1337279468 for sector 39, showing all Gaia sources brighter than  $G = 21$  mag. There are three nearby field stars (TIC 1337279457, TIC 1337279471, and TIC 1337279458), all with separations of  $\sim 4''$ – $5''$  and magnitude differences  $\Delta T = 5.5$ – $6$  mag each (marked with dashed red arrows). None of them is bright enough to produce any of the eclipses seen in the target’s lightcurve. The coordinates, parallax, and proper motion for TIC 1337279468 and TIC 1337279471 are within  $\sim 1\sigma$ , suggesting a potential comoving septuple system.

significant astrometric excess noise (e.g., Belokurov et al. 2020; Penoyre et al. 2021).

#### 5.4.3. Ephemerides Crossmatch with TESS Eclipsing Binaries

For completeness, we perform a preliminary comparison between each set of ephemerides for each quadruple candidate presented here to those of a sample of 31,154 EB candidates (unvetted) from the GSFC EB Catalog (E. Kruse et al. 2022, in preparation).

Restricting the ephemerides match to a  $10^{-3}$  fractional difference in orbital period and  $10^{-3}$  in orbital phase, three of the quadruple candidates show close matches with targets from the GSFC TESS EB catalog (see Table 2). These are (1) TIC 63459761 versus TIC 63459765/63459804/63459811, which is due to contamination as the coordinates are very close; (2) TIC 283940788 (R.A. = 8.85, decl. = 62.90) versus TIC 285609529/285609535 (R.A. = 296.25/296.25, decl. = 26.14/26.14); and

**Table 3**Observed vs. Simulated Numbers of Systems with Period Ratios  $P_B/P_A$  within the Listed Percentage of 1:1, 5:4, 4:3, 3:2, 5:3, 2:1, 5:2, and 3:1

Percentage	Observed	Simulated
1%	7	$6 \pm 2$
2%	13	$12 \pm 3$
4%	24	$25 \pm 4$
8%	47	$50 \pm 6$

(3) TIC 370440624 (R.A. = 143.23, decl. =  $-68.68$ ) versus TIC 451982722/451982756 (R.A. = 296.58/296.58, decl. = 27.06/27.06). Assuming no cross-talk between distant TESS pixels, targets (2) and (3) are due to coincidence as the corresponding sky coordinates are quite different. While a comprehensive crossmatch is beyond the scope of this work, it could be performed once the GSFC FFI EB catalog is released and fully vetted (E. Kruse et al. 2022, in preparation).

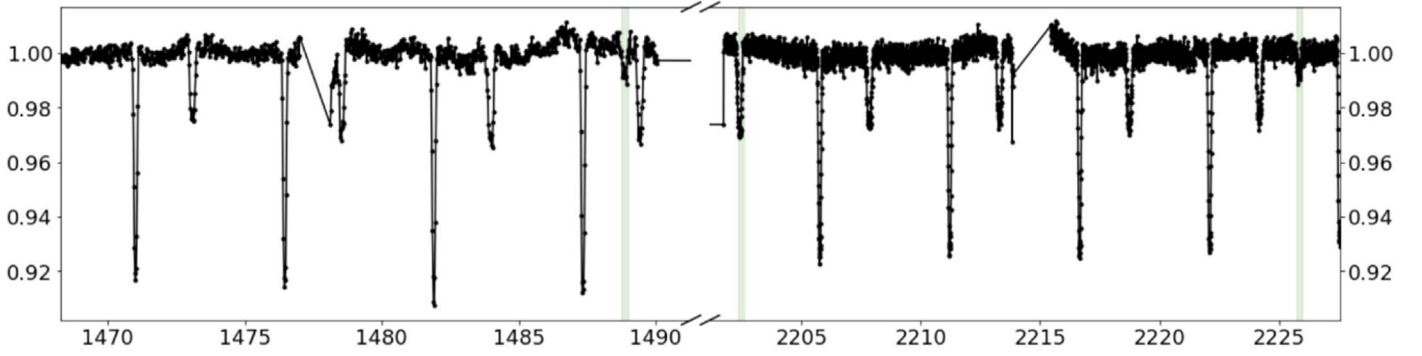
#### 5.4.4. Different Data Sets, Different Lightcurves

During our visual examination of *eleanor* and QLP lightcurves, we have noticed that sometimes there are distinct differences between the two data sets. As another potential source of false positives, it is important to keep track of such differences and investigate their source.

An example is shown in Figure 26 for the case of TIC 13120007, where there are clear eclipses in QLP data but no discernible features in *eleanor* data. Note that the sector 15 eclipses in QLP data have notably different depths before and after the data gap, which is a potential indicator for a false positive. The photocenter vetting analysis discussed above cannot be applied to *eleanor* data as there are no eclipses. However, in cases like this we use the pixel-by-pixel *eleanor* data to vet the target. Here the data show that the target is not the source of the signal and the EB is in fact off target, about 2 pixels away.

Another example is shown in Figure 27 for the case of TIC 63708251. Here the *eleanor* lightcurve shows one set of eclipses, whereas QLP shows two sets of eclipses. As in the case of TIC 13120007, we cannot perform photocenter analysis of the *eleanor* data for the shallow eclipses. However, as seen from Figure 27, the pixel-by-pixel *eleanor* data show that only the deeper eclipses seen in both data sets are on target, whereas the second EB seen in the QLP data is off target, about 5 pixels away. Interestingly, there is a third EB in the target’s  $13 \times 13$  pixel TESS aperture, near the upper right corner.





**Figure 24.** Lightcurve of TIC 438226195, highlighting the extra events in sectors 6 and 33 (first and last green vertical bands) that mimic a circumbinary planet. Close inspection shows that the two events are due to a second EB with a period of  $\sim 11.7$  days, with a third event blended with the first secondary eclipse in sector 33 (second vertical green band), slightly deeper compared with the other secondaries in sector 33.

**Table 4**

Quadruple Candidates Brighter than  $T_{\text{mag}} = 12$  and Eclipse Depths Greater than 1% (Sorted by Magnitude)

TIC	$T_{\text{mag}}$	Depth <sub>A</sub> (%)	Depth <sub>B</sub> (%)
97356407	6.46	2	14
357810643	7.03	2	8
344541836	7.77	4	3
367448265	7.83	2	20
200094011	8.66	18	23
146810480	8.67	2	13
470710327	9.23	6	7
257776944	9.42	12	3
286470992	9.60	2	20
307119043	9.77	7	9
311838200	9.82	15	5
260056937	9.85	23	2
454140642	9.85	10	10
278352276	10.00	12	8
317863971	10.24	14	6
250119205	10.25	5	8
461614217	10.32	2	7
392229331	10.34	15	14
255532033	10.34	14	8
389836747	10.36	18	2
139944266	10.36	1	4
399492452	10.39	0	21
434452777	10.56	7	7
73296637	10.57	1	2
328181241	10.57	15	17
439511833	10.58	4	8
414026507	10.61	7	13
52856877	10.62	22	20
322727163	10.65	4	11
139650665	10.74	11	3
123098844	10.79	4	8
168789840	10.80	1	4, 6
204698586	10.84	4	12
309025182	10.87	8	11
89278612	10.88	5	11
79140936	10.90	2	40
63459761	10.93	2	7
274791367	10.97	11	11
78568780	11.05	6	3
408147984	11.10	6	2
239872462	11.14	6	6
25818450	11.14	1	8
314802266	11.18	7	26
370440624	11.34	5	5
125952257	11.36	14	3

**Table 4**

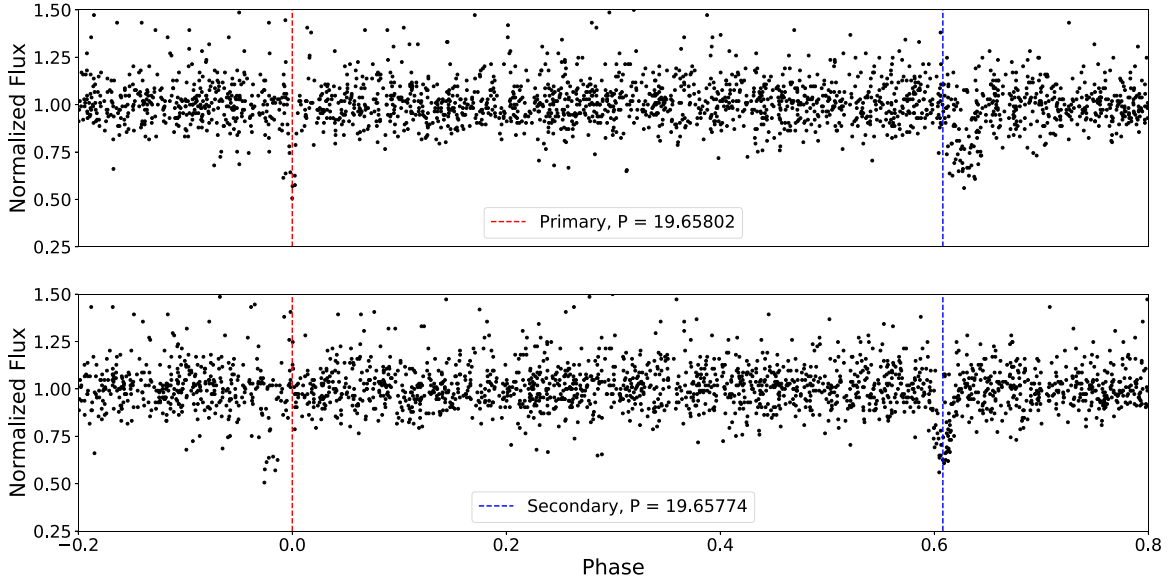
(Continued)

TIC	$T_{\text{mag}}$	Depth <sub>A</sub> (%)	Depth <sub>B</sub> (%)
336882813	11.40	1	6
348651800	11.40	1	6
283940788	11.47	3	16
251757935	11.51	11	11
266771301	11.51	1	0
284814380	11.54	18	7
178953404	11.62	4	11
190895730	11.63	8	4
264402353	11.65	2	1
271186951	11.78	8	28
414475823	11.79	14	21
285681367	11.80	14	13
141733685	11.82	1	8, 22
321471064	11.91	8	6
161043618	11.91	8	5
130276377	11.93	7	4
391620600	11.95	9	2
285655079	11.96	22	11
9493888	11.98	15	9
427092089	11.98	1	1

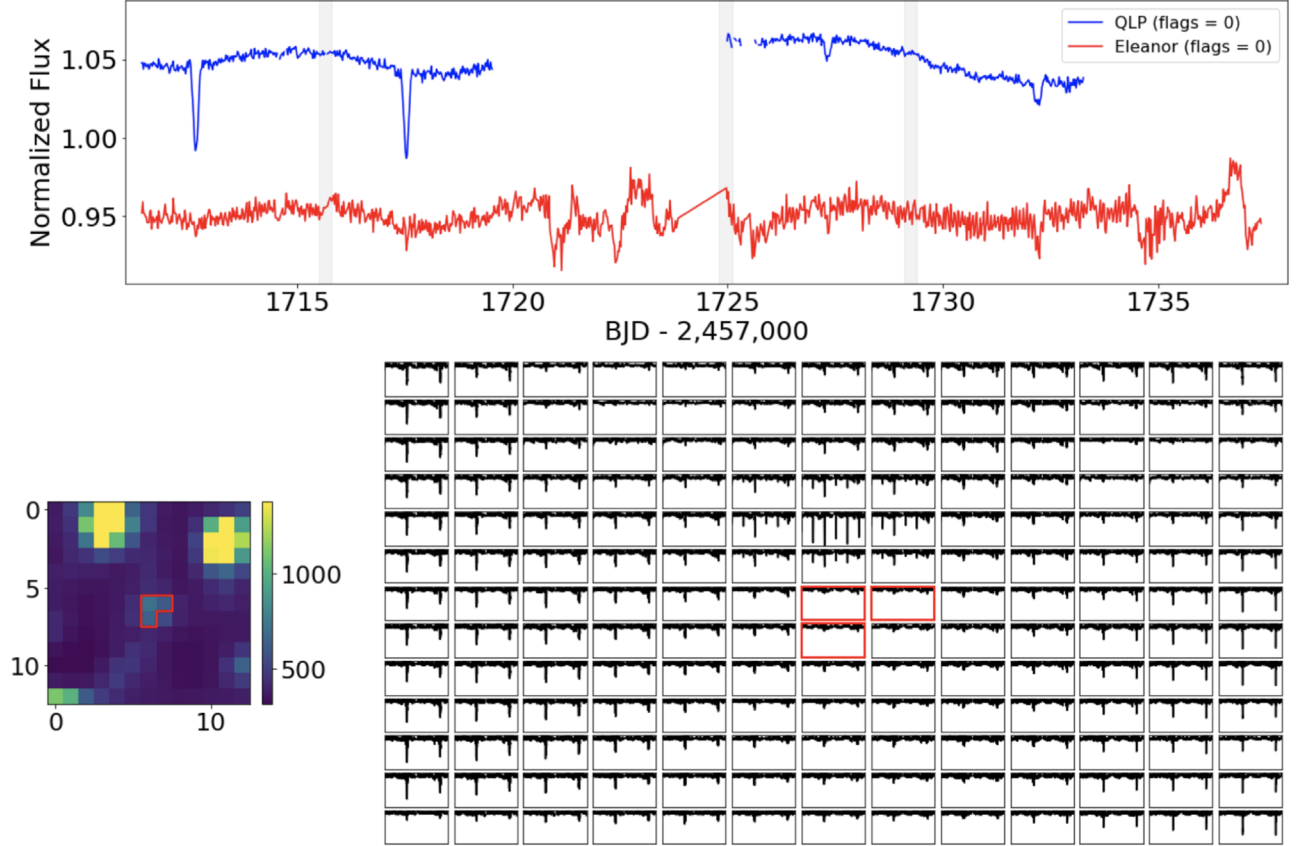
#### 5.4.5. Quadruple Stars from TESS

Our group has visually inspected millions of TESS lightcurves produced by several different pipelines. These include (1)  $\approx 2.2$  million *eleonor* lightcurves (B. Powell et al. 2022, in preparation) for sectors 1–40; (2) all TESS candidate target list (Stassun et al. 2019) short-cadence lightcurves for sectors 1–42; (3) QLP lightcurves for sectors 2–4, 9, 13–27, 35 (Huang et al. 2020); (4) (Oelkers & Stassun 2018) lightcurves for sectors 1–5; (5) CDIPS FFI lightcurves for sectors 6–13 (Bouma et al. 2020); (6) PATHOS sector 4–14 lightcurves (Nardiello et al. 2019). Altogether, the different lightcurve sets include targets as faint as  $T = 15$  mag and thus represent a significant portion of all available TESS data.

Using these lightcurves, at the time of submission we have detected 2311 candidates for multiple stellar systems (triple and higher order). Of these, 1319 ( $\sim 57\%$ ) have been already vetted such that (1) 10% passed all vetting tests; (2) 9% passed preliminary vetting tests, including the analysis of the pixel-by-pixel data; and (3) 81% were ruled out as false positives. The catalog of 97 quadruple candidates presented here represents all



**Figure 25.** Phase-folded DASCH data of TIC 172900988—an EB hosting a transiting circumbinary planet. The upper panel shows the data folded on the primary eclipse (dashed red line), and the lower panel shows the data folded on the secondary eclipse (dashed blue line). The two eclipses follow slightly different periods due to the apsidal motion of the binary caused by dynamical perturbation from the planet.

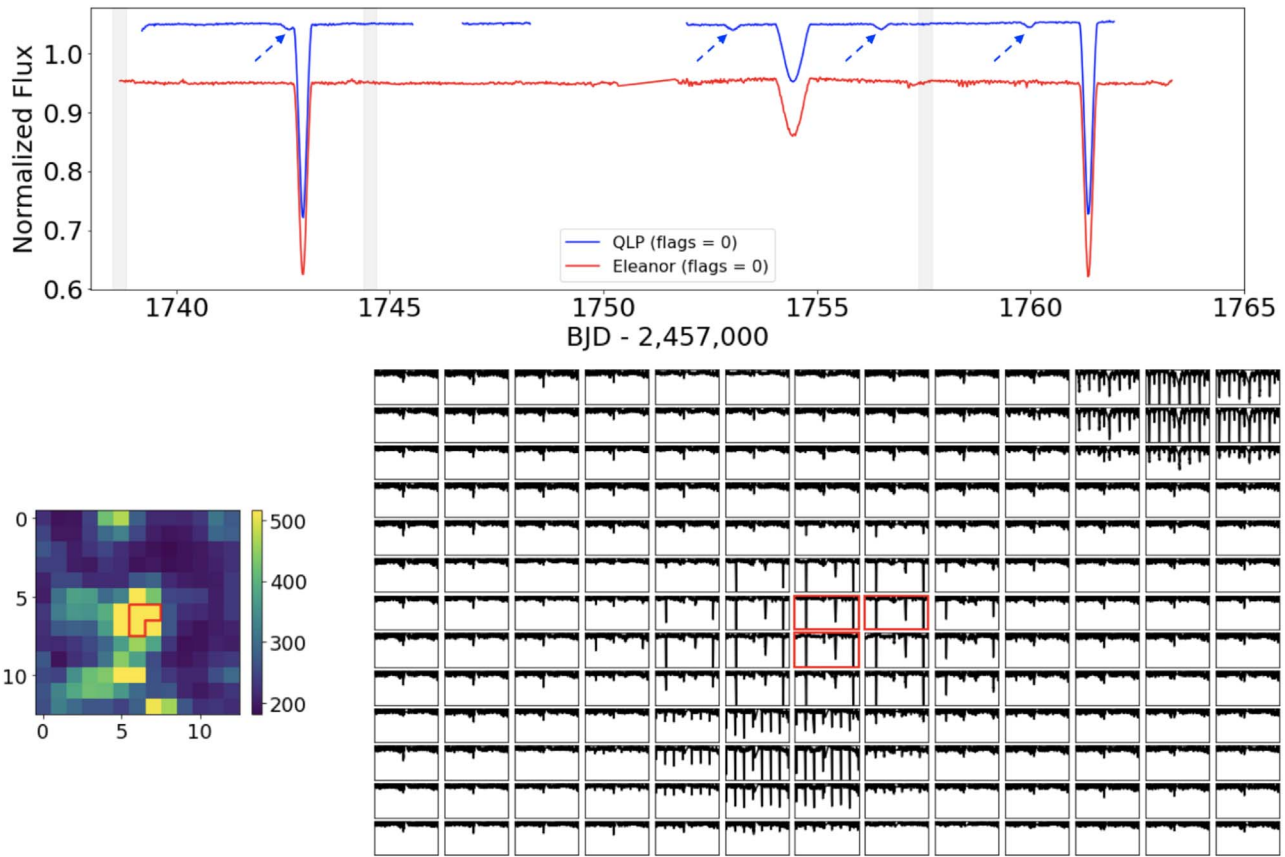


**Figure 26.** Upper panel: *eleanor* (red) and QLP (blue) lightcurves for TIC 13120007, showing clear eclipses in the latter but no eclipses in the former. The vertical gray bands indicate momentum dumps. Lower left panel: TESS’s  $13 \times 13$  pixel field of view centered on the target. The red contour indicates the aperture used by *eleanor* to extract the lightcurve. Lower right panel: pixel-by-pixel *eleanor* data for TIC 13120007 showing that the source of the EB is 2 pixels above the target.

such fully vetted systems except the handful that need further analysis. There are 905 candidates ( $\sim 39\%$ ) that still need to be vetted, and the nature of 87 candidates (4%) is currently unclear. Overall, the detection, vetting, and analysis of our candidates is a continuous process, and we plan to present the results in a series

of papers. To facilitate follow-up observations, we list in Table 4 those quadruple candidates presented here that are brighter than  $T_{\text{mag}} = 12$  and have eclipse depths greater than 1%.

The number of false positives we have encountered is more than an order of magnitude larger than the number of fully



**Figure 27.** Same as Figure 26 but for TIC 63708251. A potential quadruple candidate in QLP data (see blue curve in upper panel and blue arrows), which is a false positive due to a nearby EB located about 5 pixels below the target. The vertical gray bands indicate momentum dumps. We note that there is another EB in the upper right corner of the pixel field of view.

vetted quadruple candidates presented here. Thus while completeness analysis is beyond the scope of this work, given the large number of targets inspected and assuming many of the additional candidates turn out to be real, TESS has the potential to increase the number of known eclipsing quadruple systems by more than a factor of 2.

## 6. Summary

We have presented a catalog of 97 eclipsing quadruple star candidates detected in TESS FFIs. The target stars have been identified through visual inspection and exhibit two sets of eclipses with two distinct periods, each with primary and, in most cases, secondary eclipses. All targets have been uniformly vetted and passed a series of tests, including pixel-by-pixel and photocenter motion analysis. We outlined the procedures for determining orbital periods, eclipse depths, and durations and discussed the statistical properties of the sample.

We thank the referee for the insightful comments which helped improve this article. This paper includes data collected by the TESS mission, which are publicly available from the Mikulski Archive for Space Telescopes (MAST). Funding for the TESS mission is provided by NASA’s Science Mission directorate.

Resources supporting this work were provided by the NASA High-End Computing (HEC) Program through the NASA Center for Climate Simulation (NCCS) at Goddard Space Flight Center. Personnel directly supporting this effort were Mark L. Carroll, Laura E. Carriere, Ellen M. Salmon, Nicko D.

Acks, Matthew J. Stroud, Bruce E. Pfaff, Lyn E. Gerner, Timothy M. Burch, and Savannah L. Strong.

This research has made use of the Exoplanet Follow-up Observation Program website, which is operated by the California Institute of Technology, under contract with the National Aeronautics and Space Administration under the Exoplanet Exploration Program.

This research is based on observations made with the Galaxy Evolution Explorer, obtained from the MAST data archive at the Space Telescope Science Institute, which is operated by the Association of Universities for Research in Astronomy, Inc., under NASA contract NAS5-26555.

T.B. acknowledges the financial support of the Hungarian National Research, Development and Innovation Office—NKFIH grant KH-130372. V.B.K. is thankful for support from NASA grants 80NSSC21K0631 and 80NSSC21K0351.

This work has made use of data from the European Space Agency (ESA) mission Gaia (<https://www.cosmos.esa.int/gaia>), processed by the Gaia Data Processing and Analysis Consortium (DPAC, <https://www.cosmos.esa.int/web/gaia/dpac/consortium>). Funding for the DPAC has been provided by national institutions, in particular the institutions participating in the Gaia Multilateral Agreement.








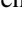








Resources supporting this work were provided by the NASA High-End Computing (HEC) Program through the NASA Advanced Supercomputing (NAS) Division at Ames Research Center for the production of the SPOC data products.

This work makes use of observations from the LCOGT network.

**Facilities:** Gaia, MAST, TESS, WASP, ASAS-SN, NCCS, FRAM, PEST, CHIRON, TRES, SOAR, LCOGT.

**Software:** Astrocut (Brasseur et al. 2019), AstroImageJ (Collins et al. 2017), Astropy (Astropy Collaboration et al. 2013, 2018), Eleanor (Feinstein et al. 2019), IPython (Pérez & Granger 2007), Keras (Chollet et al. 2015), LcTools (Schmitt et al. 2019; Schmitt & Vanderburg 2021), Lightcurvefactory (Borkovits et al. 2013; Rappaport et al. 2017; Borkovits et al. 2018), Lightkurve (Lightkurve Collaboration et al. 2018), Matplotlib (Hunter 2007), Mpi4py (Dalcin et al. 2008), NumPy (Harris et al. 2020), Pandas (McKinney 2010), PHOEBE (Prsa et al. 2011), Scikit-learn (Pedregosa et al. 2011), SciPy (Virtanen et al. 2020), Tensorflow (Abadi et al. 2015), Tess-point (Burke et al. 2020) wotan (Hippke et al. 2019).

## ORCID iDs

Veselin B. Kostov  <https://orcid.org/0000-0001-9786-1031>  
 Brian P. Powell  <https://orcid.org/0000-0003-0501-2636>  
 Saul A. Rappaport  <https://orcid.org/0000-0003-3182-5569>  
 Tamás Borkovits  <https://orcid.org/0000-0002-8806-496X>  
 Robert Gagliano  <https://orcid.org/0000-0002-5665-1879>  
 Thomas L. Jacobs  <https://orcid.org/0000-0003-3988-3245>  
 Martti H. Kristiansen  <https://orcid.org/0000-0002-2607-138X>  
 Daryll M. LaCourse  <https://orcid.org/0000-0002-8527-2114>  
 Jerome Orosz  <https://orcid.org/0000-0001-9647-2886>  
 Allan R. Schmitt  <https://orcid.org/0000-0002-5034-0949>  
 Guillermo Torres  <https://orcid.org/0000-0002-5286-0251>  
 Thomas Barclay  <https://orcid.org/0000-0001-7139-2724>  
 Ethan Kruse  <https://orcid.org/0000-0002-0493-1342>  
 Greg Olmschenk  <https://orcid.org/0000-0001-8472-2219>  
 Andrew Vanderburg  <https://orcid.org/0000-0001-7246-5438>  
 William Welsh  <https://orcid.org/0000-0003-2381-5301>

## References

- Abadi, M., Agarwal, A., Barham, P., et al. 2015, TensorFlow: Large-Scale Machine Learning on Heterogeneous Systems, <https://www.tensorflow.org/>  
 Astropy Collaboration, Price-Whelan, A. M., Sipőcz, B. M., et al. 2018, *AJ*, **156**, 123  
 Astropy Collaboration, Robitaille, T. P., Tollerud, E. J., et al. 2013, *A&A*, **558**, A33  
 Bakos, G., Noyes, R. W., Kovács, G., et al. 2004, *PASP*, **116**, 266  
 Belokurov, V., Penoyre, Z., Oh, S., et al. 2020, *MNRAS*, **496**, 1922  
 Borkovits, T., Albrecht, S., Rappaport, S., et al. 2018, *MNRAS*, **478**, 5135  
 Borkovits, T., Derekas, A., Kiss, L. L., et al. 2013, *MNRAS*, **428**, 1656  
 Borkovits, T., Hajdu, T., Sztakovics, J., et al. 2016, *MNRAS*, **455**, 4136  
 Borucki, W. J., Koch, D., Basri, G., et al. 2010, *Sci*, **327**, 977  
 Bouma, L. G., Hartman, J. D., Bhatti, W., Winn, J. N., & Bakos, G. A. 2020, *yCat*, *JApJS*, **245**, 13  
 Brasseur, C. E., Phillip, C., Fleming, S. W., Mullally, S. E., & White, R. L. 2019, Astrocut: Tools for creating cutouts of TESS images, Astrophysics Source Code Lib, ascl:1905.007  
 Breiter, S., & Vokrouhlický, D. 2018, *MNRAS*, **475**, 5215  
 Burke, C. J., Levine, A., Fausnaugh, M., et al. 2020, TESS-Point: High precision TESS pointing tool, Astrophysics Source Code Library, ascl:2003.001  
 Chollet, F., et al. 2015, Keras, <https://keras.io>  
 Collins, K. A., Kielkopf, J. F., Stassun, K. G., & Hessman, F. V. 2017, *AJ*, **153**, 77  
 Dalcin, L., Paz, R., Storti, M., & D'Elia, J. 2008, *JPDC*, **68**, 655  
 Fang, X., Thompson, T. A., & Hirata, C. M. 2018, *MNRAS*, **476**, 4234  
 Feinstein, A. D., Montet, B. T., Foreman-Mackey, D., et al. 2019, *PASP*, **131**, 094502  
 Fragione, G., & Kocsis, B. 2019, *MNRAS*, **486**, 4781  
 Fűrész, G. 2008, PhD thesis, University of Szeged  
 Gaia Collaboration, Brown, A. G. A., Vallenari, A., et al. 2021, *A&A*, **649**, A1  
 Gandhi, P., Buckley, D. A. H., Charles, P. A., et al. 2022, *MNRAS*, **510**, 3885  
 Grindlay, J., Tang, S., Los, E., & Servillat, M. 2012, in IAU Symp. 285, New Horizons in Time Domain Astronomy, ed. E. Griffin, R. Hanisch, & R. Seaman (Cambridge: Cambridge Univ. Press), 29  
 Hamers, A. S., Rantala, A., Neunteufel, P., Preece, H., & Vynatheya, P. 2021, *MNRAS*, **502**, 4479  
 Harris, C. R., Millman, K. J., van der Walt, S. J., et al. 2020, *Natur*, **585**, 357  
 Hattori, S., Foreman-Mackey, D., Hogg, D., Schölkopf, B., & Pritchard, T. 2020, AAS Meeting, **235**, 157.05  
 He, K., Zhang, X., Ren, S., & Sun, J. 2015, arXiv:1512.03385  
 Hippke, M., David, T. J., Mulders, G. D., & Heller, R. 2019, *AJ*, **158**, 143  
 Huang, C. X., Vanderburg, A., Pál, A., et al. 2020, *RNAAS*, **4**, 204  
 Hunter, J. D. 2007, *CSE*, **9**, 90  
 Kochanek, C. S., Shappee, B. J., Stanek, K. Z., et al. 2017, *PASP*, **129**, 104502  
 Kostov, V. B., Mullally, S. E., Quintana, E. V., et al. 2019, *AJ*, **157**, 124  
 Kostov, V. B., Powell, B. P., Orosz, J. A., et al. 2021a, *AJ*, **162**, 234  
 Kostov, V. B., Powell, B. P., Torres, G., et al. 2021b, *ApJ*, **917**, 93  
 Kounkel, M., Covey, K. R., Stassun, K. G., et al. 2021, *AJ*, **162**, 184  
 Kovács, G., Zucker, S., & Mazeh, T. 2002, *A&A*, **391**, 369  
 Kozai, Y. 1962, *AJ*, **67**, 591  
 Kristiansen, M., Rappaport, S., Vandenburg, A., et al. 2022, *PASP*, submitted  
 Lidov, M. L. 1962, *P&SS*, **9**, 719  
 Lightkurve Collaboration, Cardoso, J. V. D. M., Hedges, C., et al. 2018, Lightkurve: Kepler and TESS time series analysis in Python, Astrophysics Source Code Library, ascl:1812.013  
 Liu, B., & Lai, D. 2019, *MNRAS*, **483**, 4060  
 Mathieu, R. D. 1994, *ARA&A*, **32**, 465  
 McKinney, W. 2010, in Proc. of the 9th Python in Science Conf., ed. S. van der Walt & J. Millman, 51  
 Moe, M., & Di Stefano, R. 2017, *ApJS*, **230**, 15  
 Nardiello, D., Borsato, L., Piatto, G., et al. 2019, *MNRAS*, **490**, 3806  
 Oelkers, R. J., & Stassun, K. G. 2018, *AJ*, **156**, 132  
 Pál, A. 2012, *MNRAS*, **421**, 1825  
 Pedregosa, F., Varoquaux, G., Gramfort, A., et al. 2011, *J. Mach. Learn. Res.*, **12**, 2825  
 Pejcha, O., Antognini, J. M., Shappee, B. J., & Thompson, T. A. 2013, *MNRAS*, **435**, 943  
 Penoyre, Z., Belokurov, V., & Evans, N. W. 2021, arXiv:2111.10380  
 Penoyre, Z., Belokurov, V., Wyn Evans, N., Everall, A., & Koposov, S. E. 2020, *MNRAS*, **495**, 321  
 Pepper, J., Pogge, R. W., DePoy, D. L., et al. 2007, *PASP*, **119**, 923  
 Pérez, F., & Granger, B. E. 2007, *CSE*, **9**, 21  
 Pineda, J. E., Offner, S. S. R., Parker, R. J., et al. 2015, *Natur*, **518**, 213  
 Pollacco, D. L., Skillen, I., Collier Cameron, A., et al. 2006, *PASP*, **118**, 1407  
 Powell, B. P., Kostov, V. B., Rappaport, S. A., et al. 2021, *AJ*, **161**, 162  
 Prsa, A., Matijevic, G., Latkovic, O., Vilardell, F., & Wils, P. 2011, PHOEBE: PHysics Of Eclipsing BinariEs, Astrophysics Source Code Library, ascl:1106.002  
 Raghavan, D., McAlister, H. A., Henry, T. J., et al. 2010, *ApJS*, **190**, 1  
 Rappaport, S., Lehmann, H., Kalomeni, B., et al. 2016, *MNRAS*, **462**, 1812  
 Rappaport, S., Vanderburg, A., Borkovits, T., et al. 2017, *MNRAS*, **467**, 2160  
 Schmitt, A., & Vanderburg, A. 2021, arXiv:2103.10285  
 Schmitt, A. R., Hartman, J. D., & Kipping, D. M. 2019, arXiv:1910.08034  
 Shappee, B. J., Prieto, J. L., Grupe, D., et al. 2014, *ApJ*, **788**, 48  
 Stassun, K. G., Oelkers, R. J., Paegert, M., et al. 2019, *AJ*, **158**, 138  
 Stassun, K. G., & Torres, G. 2021, *ApJL*, **907**, L33  
 Szentgyorgyi, A. H., & Fűrész, G. 2007, *RMxAC*, **28**, 129  
 Tobin, J. J., Kratter, K. M., Persson, M. V., et al. 2016, *Natur*, **538**, 483  
 Tokovinin, A. 2018, *ApJS*, **235**, 6  
 Tokovinin, A. 2021, *Univ*, **7**, 352  
 Tremaine, S. 2020, *MNRAS*, **493**, 5583  
 Udalski, A., Szymanski, M., Kaluzny, J., Kubiak, M., & Mateo, M. 1992, *AcA*, **42**, 253  
 Virtanen, P., Gommers, R., Oliphant, T. E., et al. 2020, *NatMe*, **17**, 261  
 Whitworth, A. P. 2001, in IAU Symp. 200, The Formation of Binary Stars, ed. H. Zinnecker & R. Mathieu (San Francisco, CA: ASP), 33  
 Woźniak, P. R., Vestrand, W. T., Akerlof, C. W., et al. 2004, *AJ*, **127**, 2436  
 Zasche, P., Vokrouhlický, D., Wolf, M., et al. 2019, *A&A*, **630**, A128